
Article:

Fu, T, Yang, J, Li, Q et al. (2020) Groupwise registration with global-local graph shrinkage in atlas construction. Medical Image Analysis, 64. 101711. ISSN: 1361-8415

https://doi.org/10.1016/j.media.2020.101711

Elsevier Editorial System(tm) for Medical Image Analysis
Manuscript Draft

Manuscript Number: MEDIA-D-18-00117

Title: Groupwise Registration with Global-local Graph Shrinkage in Atlas Construction

Article Type: Research Paper

Keywords: Groupwise registration; Atlas construction; Graph shrinkage; Global-local

Corresponding Author: Professor Jian Yang, Ph.D

Corresponding Author's Institution: Beijing Institute of Technology

First Author: Tianyu Fu, Ph.D

Order of Authors: Tianyu Fu, Ph.D; Jian Yang, Ph.D; Qin Li; Danni Ai, Ph.D; Hong Song, Ph.D; Yurong Jiang, Ph.D; Yongtian Wang, Ph.D; Alejandro F Frangi, Professor

Abstract: Graph-based groupwise registration methods are widely used in atlas construction. Given a group of images, a graph is built whose nodes represent the images, and whose edges represent a geodesic path between two nodes. Distribution of images on the image manifold is explored through edge traversal in the graph. The final atlas is a mean image at the population center of the distribution on the manifold. The procedure of warping all images to the mean image turns to dynamic graph shrinkage in which nodes become close to each other. Most conventional groupwise registration frameworks construct and shrink the graph without considering the local distribution of the images on the dataset manifold and local structure variations between image pairs. Neglecting local information regarding data distribution and image similarity fundamentally compromises accuracy and computational time when population atlases are being built for organs with large inter-subject anatomical variability. To overcome this problem, this paper proposes a global-local graph shrinkage approach that can generate accurate atlases rapidly. A connected graph is constructed automatically based on global similarities across the images to explore the global distribution. A local image distribution obtained using image clustering is used to simplify the edges of the constructed graph. Subsequently, local image similarities refine the deformation estimated through global image similarity for each image warping along the graph edges. Through the proposed warping, the overall simplified graph gradually shrinks, respecting both global and local features, and with the final atlas as the result. The proposed method is evaluated on 61 synthetic and 20 clinical liver datasets, and the results are then compared with those of six state-of-the-art groupwise registration methods. The experimental results show that the proposed method outperforms non-global-local methods approaches in being faster and 70% more accurate.

Groupwise Registration with Global-local Graph Shrinkage in Atlas Construction

Tianyu Fu[1,2], Jian Yang[2]*, Qin Li[1], Danni Ai[2], Hong Song[3], Yurong Jiang[2], Yongtian Wang[2], Alejandro F. Frangi[4], *IEEE Fellow*

1. School of Life Science, Beijing Institute of Technology, Beijing 100081, China.
2. Beijing Engineering Research Center of Mixed Reality and Advanced Display, School of Optics and Photonics, Beijing Institute of Technology, Beijing 100081, China.
3. School of Software, Beijing Institute of Technology, Beijing 100081, China.
4. Center for Computational Imaging and Simulation Technologies in Biomedicine (CISTIB), Department of Electronic and Electrical Engineering, University of Sheffield, Sheffield S1 3JD, UK.

* corresponding author (Jian Yang, E-mail: jyang@bit.edu.cn.)

Abstract—Graph-based groupwise registration methods are widely used in atlas construction. Given a group of images, a graph is built whose nodes represent the images, and whose edges represent a geodesic path between two nodes. Distribution of images on the image manifold is explored through edge traversal in the graph. The final atlas is a mean image at the population center of the distribution on the manifold. The procedure of warping all images to the mean image turns to dynamic graph shrinkage in which nodes become close to each other. Most conventional groupwise registration frameworks construct and shrink the graph without considering the local distribution of the images on the dataset manifold and local structure variations between image pairs. Neglecting local information regarding data distribution and image similarity fundamentally compromises accuracy and computational time when population atlases are being built for organs with large inter-subject anatomical variability. To overcome this problem, this paper proposes a global-local graph shrinkage approach that can generate accurate atlases rapidly. A connected graph is constructed automatically based on global similarities across the images to explore the global distribution. A local image distribution obtained using image clustering is used to simplify the edges of the constructed graph. Subsequently, local image similarities refine the deformation estimated through global image similarity for each image warping along the graph edges. Through the proposed warping, the overall simplified graph gradually shrinks, respecting both global and local features, and with the final atlas as the result. The proposed method is evaluated on 61 synthetic and 20 clinical liver datasets, and the results are then compared with those of six state-of-the-art groupwise registration methods. The experimental results show that the proposed method outperforms non-global-local methods approaches in being faster and 70% more accurate.

Keywords—Groupwise registration, Atlas construction, Graph shrinkage, Global-local

1. Introduction

Computational atlases are a cornerstone in statistical analysis of biological variation in clinical trials and population imaging studies. Atlases provide reference frames for comparing groups and populations, and they contribute useful prior information regarding anatomy and function for other medical image computing tasks [1-5]. Analyzing population imaging data by registering a group of images can assist in highlighting meaningful functional and structural disparities between subject groups or over time, [6-8]. Previous studies on population imaging analysis have applied groupwise registrations to construct atlases of various organs [9]. However, only a few studies have reported the successful application of these approaches in registering large image sets of deformable visceral organs (e.g. liver) involving wide anatomical variability. Registering high-dimensional inter-subject organs with large anatomical differences to a common space is time-consuming and produces errors in the deformation estimation. Therefore, accurate and rapid analysis would be of substantial value for population data.

Groupwise registration registers a group of images to a common space to obtain an atlas. Groupwise registration using a dynamic template image has been proposed to guide groupwise registration without a specific template. Group-mean-based approaches [10, 11] generate a group mean image as a template for registration in each iteration. The group mean image is a linear average of all images in the group, and all images are directly registered to the template image until the differences between the images are small. Given large differences across images in a group, the initial group mean image is not sufficiently sharp to achieve an accurate registration between each image in the population and the initial group-mean image. The fuzzy mean image used in Group-mean-based methods leads to an unrecoverable information loss [9] in anatomical structure. To compensate for performance loss, a sharp mean image computed in SharpMean [12] is treated as an alternative to the fuzzy group mean image in each iteration. In [12], the weight of each image for averaging is adjusted adaptively to generate a sharp mean image. The weights are computed according to the difference between the mean image acquired from the previous iteration and each image inside the dataset. In the initial iteration, the image with the closest distance to other images is selected as the initial mean image. The sharp mean image is a template image used to guide the registration of other images. Although a sharp mean image is provided for groupwise registration, the atlas obtained by SharpMean is of a limited accuracy as a result of directly registering images with large differences. Hoogendoorn et al. proposed the groupwise mutual information-based method (GWMI) for estimating a high-resolution atlas [13]. This method uses groupwise mutual information to compare a single image with other images in the dataset. The single image having the largest value of groupwise mutual information is close to the mean of the population and is selected as a template. All images are directly registered to the template image and the corresponding deformations are estimated. The estimated deformations are then averaged linearly to obtain a mean deformation. The template image is warped and updated by the mean deformation until the mean deformation is an identity deformation, and the updated template image guides the registration of the images in the dataset. Tang et al. proposed a method [14] based on dynamic directed graphs (DDG), in which a graph can be built using the minimum spanning tree (MST), and the edges are weighted by the differences between images. An image in the population with the shortest path between it and other images is taken as the root image in the graph, and the non-root images are registered to the corresponding parent images in the graph. The differences between images change in each iteration. DDG are used to guide the groupwise registrations of the images. All non-root images are registered to the root image along the edges in the DDG. Unlike methods that directly register the images to a template image, [14] registers the images with their parent images as intermediate templates to achieve higher accuracy [15]. Shen et al. [9] proposed the atlas building by self-organized registration and bundling (ABSORB) algorithm, the critical step in which is the determination of the neighborhood for each image per iteration. This determination is associated with a tentatively estimated template image and distribution of the image. That template image is the median image on the learned manifold, which is positioned close to the final atlas which is the population center of the distribution on the learned manifold. Each image is warped toward its neighbors closest to the distribution center. However, the neighborhood for each image is selected regardless of the global distribution of the overall images. Through iterations, several nearby images converge spontaneously, and the image set is partitioned into sub-groups. The multiple sub-groups cannot construct an accurate atlas for the image set [11], and template-based groupwise registrations, such as ABSORB, are potentially biased toward the selected or estimated dynamic template image.

Groupwise registration without a template offers a great advantage in no longer requiring the selection or estimation of a template image. Hierarchical unbiased graph shrinkage (HUGS) [16] was proposed to compute an atlas using an undirected graph without a template. In this method, distributing the images in a dataset is modeled in terms of an undirected graph in which each image is a node and each edge represents a geodesic pathway between two nodes. To avoid the convergence to multiple sub-groups through iterations, the edges in the graph are selected by a threshold to link all images with the global distribution of the dataset. And the threshold is optimized by line-search. In line-search process, both step size and precision must be manually specified to adapt for the input dataset. An undirected graph is then constructed based on the selected edges, and the global distribution on an image manifold is modeled via the graph. All images are registered along the edges, and the corresponding deformations are estimated. For each image in the dataset, the estimated deformations between it and the connected images are averaged with global weights. Each image is warped by the average deformation. Through iterations, the difference between the images decreases and the graph shrinks to a population center, which is the final atlas [9, 12, 16]. HUGS avoids the potential bias resulting from template selection or estimation by using the global distribution. However, given that optimization is based on the global data distribution of the image set, a common threshold for an entire dataset might be suboptimal. Neglecting local data distributions, an inappropriate threshold might increase the number of edges and lead to redundant registrations. An excess of image registrations can result in averaging too many deformations, which can weaken the deformations toward the final atlas and decelerate the convergence process. Meanwhile, image warping with global weights is less sensitive or ignores local differences between images linked in the graph. Considerable inter-subject variations can affect the accuracy of the final atlas [16].

This paper proposes a novel groupwise registration method in which a graph and its shrinkage are refined through the use of global-local information at two levels. The first level is the global-local information of the image distribution on the manifold. A connected graph is constructed to model the global distribution. A basic node in this graph represents an individual image, and an edge represents the geodesic pathway between two such images. Edges in the graph are pruned using image clustering by temporarily storing local image distributions within each class. The second level accounts for global-local image structure similarities. At this level, deformation estimation is achieved using image- and patch-wise registrations that capture global-local similarities between the linked images. To build the final atlas, we warp each image by the mean of all inflowing estimated deformations at the corresponding node and traverse the graph shrinkage accumulating the warps.

The main contributions of this work are summarized: (1) a graph is automatically constructed to model the global distribution of the dataset on the image manifold without a priori templates; (2) higher computational efficiency through requiring fewer edges is achieved by maintaining the local distributions on the image manifold; (3) improved accuracy of the resultant atlas by capturing both global and local variations of each image on the manifold in the graph shrinkage process.

The remainder of this paper is summarized as follows. The method section explains the construction and mathematical formulation of the weighted shrinkage of the simplified graph. The experiment section discusses the theoretical derivation and systematically evaluates the performance of the proposed method using synthetic and clinical datasets. The results of the proposed method are then compared with those of Group-mean, GWMI, DDG, ABSORB, SharpMean, and HUGS. The discussion section presents the analysis and evaluation results.

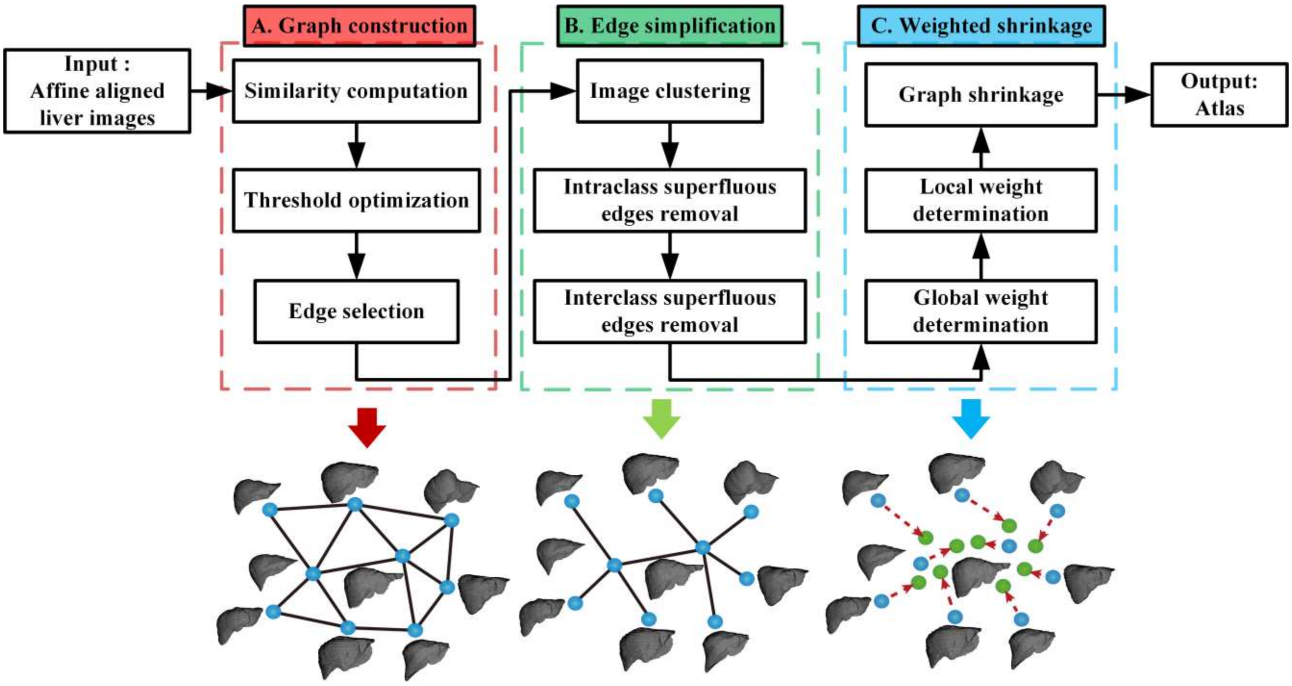

Fig. 1. Flowchart of the proposed groupwise registration method.

2. Method

Fig. 1 summarizes the proposed global-local graph shrinkage for groupwise registration. The proposed framework is divided into three principal parts, *graph construction, edge simplification,* and *weighted shrinkage*. The output of each part is shown at the bottom of Fig. 1. In *graph construction*, the affine-aligned images (e.g., liver images) are inputs for the nodes in the graph, and the similar measurements between any two images are computed. Then, a threshold is calculated using fuzzy set theory based on the similarities between the images. The edges between two images in the graph are then selected by comparing their similarities and the calculated threshold. A connected graph linking all nodes via edges is constructed. In *edge simplification,* all images are clustered into several classes to strengthen the information of local image distribution and simplify the edges in the graph. The intra- and interclass redundant edges are then removed. In *weighted shrinkage*, the global weights of the whole deformations between the directly connected images are determined. Based on the local variations, the local weights are computed and used to refine the whole deformation of each image in local areas. The deformations between directly connected images are averaged using the refined weights and are then used to warp the source image. Image warping reduces the differences between images, and the simplified graph gradually shrinks. All images are eventually warped to a common space, and a final atlas is obtained.

2.1 Graph construction

Let us assume that $V=\{I_i : i=1,2,\ldots N\}$ and $E=\{e_{ij} : i,j=1,2,\ldots N\}$ are the node and edge sets, respectively, while $G(V,E)$ is the associated graph. I_i is an image and *N* is the number of images in the dataset. If an edge exists between I_i and I_j, then $e_{ij}=1$; otherwise, $e_{ij}=0$. The edges provide a dynamic sequence of deformations (path) that warps each image in the dataset into the final atlas. Hence, to guide the way to an accurate atlas with the edges, the following two conditions must be satisfied [16]:

Condition 1: There is at least one path connecting any two images.

Condition 2: The number of edges in the graph is minimal.

To select the edge set *E* that satisfies the above conditions, an optimal threshold *H* is computed using a fuzzy clustering algorithm [17]. Edges are preserved if the similarities between the images are greater than or equal to *H*; otherwise, they are removed. Let R_{ij} represent the similarity between the i^{th} image I_i and the j^{th} image I_j, with $i,j\in[1,N]$. R_{ij} is computed as follows:

$$R_{ij}=\begin{cases}1-\dfrac{d(I_i,I_j)}{\max(d(I_i,I_j))} & \text{if } i\neq j\\ 1 & \text{otherwise}\end{cases} \tag{1}$$

where $d(I_i,I_j)$ is the geodesic distance between I_i and I_j on the image manifold. To compute this distance, the velocity $\tilde{v}_{ij}$ from I_i to I_j is obtained as in [18], and $\tilde{v}_{ij}$ is a constant velocity [18]. $d(I_i,I_j)$ is the norm of the velocity and is presented by $\tilde{v}_{ij}$ as follows:

$$d(I_i,I_j)=\left\|\tilde{v}_{ij}\right\| \tag{2}$$

According to the reflexive and symmetric principles in [19], $R_{ii}=1$ and $R_{ij}=R_{ji}$, with $i,j\in[1,N]$. **R** is a fuzzy binary relation with components R_{ij}. The transitive closure matrix $t(\mathbf{R})$ [19] containing **R** is the smallest relation on the image set computed as follows:

$$t(\mathbf{R})=\mathbf{R}^k \quad \text{if } \mathbf{R}^k=\mathbf{R}^k\circ\mathbf{R}^k \tag{3}$$

where *k* is a positive integer, and $\circ$ denotes the max-min composed operation [17]. The values of $t(\mathbf{R})_{ij}\in[0,1]$ are the individual components in $t(\mathbf{R})$. As a consequence of (3), $t(\mathbf{R})$ satisfies the properties of reflexivity and symmetry [20].

The different non-zero values of $t(\mathbf{R})_{ij}$ are designated as $\hat{H}_f, f=1,2,\ldots,F$ in which *F* represents the number of different non-zero values. $\hat{H}_f$ is the threshold for clustering the images. If $t(\mathbf{R})_{ij}\geq\hat{H}_f$, then images I_i and I_j are clustered in the same class, and there must be at least one path connecting them; otherwise, these images exist in separate classes with no connecting path. This setting suggests that $\min(\hat{H}_f)$ is the maximum threshold that clusters all images in the same class, and the edges selected by $\min(\hat{H}_f)$ satisfies *Conditions 1* and *2* (an example is detailed in **Appendix A**). The optimal threshold *H* is represented as $H = \min(\hat{H}_f)$.

Therefore, in **R**, if $R_{ij} \geq H$, then images I_i and I_j are connected by an edge, and $e_{ij} = 1$. $G(V, E)$ is constructed by selecting the edges linking images with similarities higher than the optimal threshold *H*. In the edge set *E*, e_{ij} is derived as follows:

$$e_{ij} = \begin{cases} 1 & \text{if } R_{ij} \geq H \\ 0 & \text{otherwise} \end{cases} \tag{4}$$

Condition 1 guarantees that $G(V, E)$ is a connected graph linking all images in the dataset together. Given that $d(I_i, I_j)$ is the distance on the image manifold, $G(V, E)$ models the global distribution of all images on the manifold. Fig. 2 shows a sample connected graph. In this figure, nine inter-subject livers are distributed on the manifold, and the edges are selected based on the distances on this manifold.

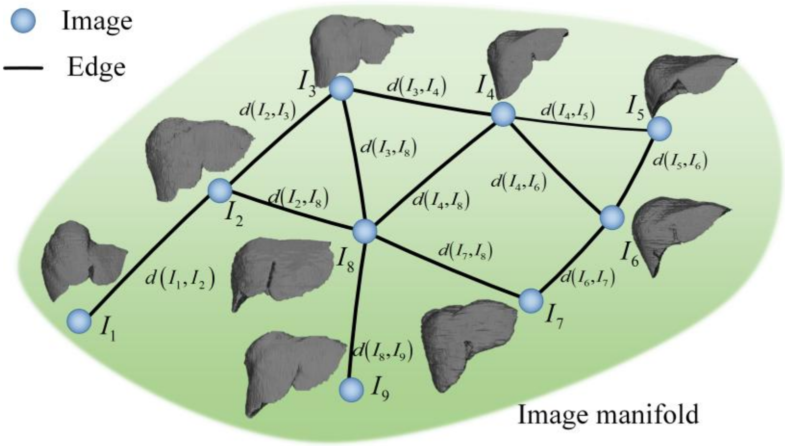

Fig. 2. Connected graph.

The optimal threshold *H* computed by the fuzzy clustering is similar to that computed in HUGS [16], which uses a line-search method. The search range in HUGS is $[0, \max(d(I_i, I_j))]$, which covers the entire domain of the differences between any two images. Meanwhile, both step size and precision in the search must be reconfigured manually in the search process to adapt to the different input datasets. The proposed method simplifies the entire line-search process by computing *H* following the fuzzy clustering principle without step size and precision.

The fuzzy clustering here is based on the global similarities across the images and is used in the graph construction to compute the threshold.

2.2 Edge simplification

The influence of specific images in the dataset that reflects features could be lost if the selected edges in the constructed graph overlook the contribution of local distribution on the image manifold. These selected edges are superfluous for the specific images. Having more edges will also lead to more registrations and a huge calculation burden. This paper proposes a novel graph simplification method based on local distributions to strengthen the local linkage and remove superfluous edges.

In contrast to the use of fuzzy clustering in *graph construction*, affinity propagation clustering [21] is used here to overcome the limitations of graphs based only on global similarities. All images are clustered into several classes, and the number of clusters is determined automatically using the affinity propagation. The superfluous edges are divided into inter- and intraclass edges. The intraclass edges are superfluous edges in the same class, while the interclass edges are superfluous edges across different classes. Based on the image clustering results, suppose that V_m is the clustered image set in the m^{th} class, E_m is the corresponding edge set between the images in V_m, and M is the number of the clustered classes. Then, $G_m(V_m, E_m)$, $(m = 1, 2, \ldots, M)$ are subgraphs associated with different classes. The set of all subgraphs is a partition of the original graph and satisfies these conditions:

$$\begin{cases} V_m \cap V_n = \varnothing \\ V_1 \cup V_2 \cup \cdots V_m = V \\ E_m \cap E_n = \varnothing \\ E_1 \cup E_2 \cup \cdots E_m \subset E \end{cases} \quad \text{if } m \neq n \text{ and } m, n = 1, 2, \ldots, M \tag{5}$$

To simplify the intraclass superfluous edges in G, the edges in each subgraph are filtered using MSTs. The edge between the images I_i and I_j in a subgraph is weighted by $d(I_i, I_j)$. An MST is a simplified subgraph $G'_m(V_m, E'_m)$ in which E'_m is the edge set in MST without redundant edges. The difference set in (6) is computed to delete all intraclass redundant edges. Then, a new graph $G'(V, E')$ can be deduced:

$$G'(V, E') = G(V, E) - \left(G_1(V_1, E_1) - G'_1(V_1, E'_1)\right) \cup \cdots \left(G_m(V_m, E_m) - G'_m(V_m, E'_m)\right) \tag{6}$$

To prune interclass superfluous edges in G, the edges between subgraphs G_m, $(m = 1, 2, \ldots, M)$ are filtered based on the connections of the class center. In G, the neighborhood set of I consists of the directly connected images. The differences between I and the directly connected images are small. The class center image identified using affinity propagation is generally near the distribution center on the manifold of the images in each class, indicating that the neighborhood of the class center must be included in the same class. If the class center image and an image in the neighborhood do not belong to the same class, the edge between them is redundant. These redundant edges will be removed. However, when the center is placed near the border of the class owing to the small number of class members, the center image in this class might be the only node connected to the other class with edges. Deleting these edges can separate the graph into two individual classes, violating *Condition 1*. Therefore, these edges must be retained to ensure connectivity between any two images in the dataset.

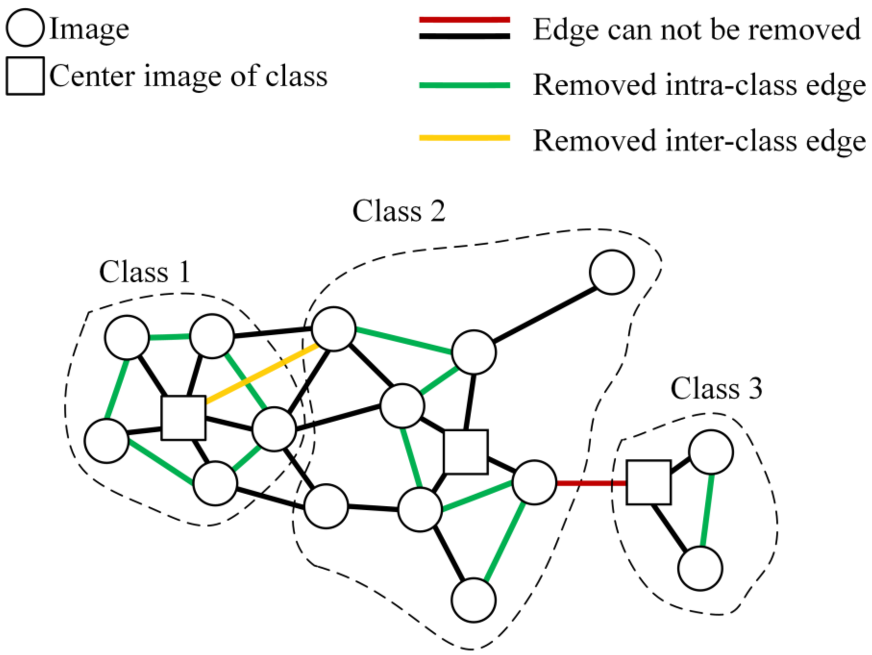

Fig. 3. Edge removal.

Based on the simplified edge set $E'\left\{e'_{ij}: i, j=1,2,\ldots N\right\}$, redundant edges across different classes are removed, and a further simplified edge set $E''\left\{e''_{ij}: i, j=1,2,\ldots N\right\}$ can be obtained as follows:

```
Algorithm  Interclass superfluous edge removal
Input:  Simplified edge set $E'$ after intraclass superfluous edge removal
Output: Simplified edge set $E''$ after interclass superfluous edge removal

$E''=E'$
For $i$=1:$N$
    For $j$=1:$N$
        If $I_i \in C$ and $NI_i \neq NI_j$, where $C$ represents the set constituted by the center
        image of each class, while $NI_i$ and $NI_j$ denote the class indices of $I_i$ and $I_j$.
            $e''_{ij}=0$
            Update $E''$
            If $E''$ do not meet Condition 1
                $e''_{ij}=1$
                Update $E''$
            End
        End
    End
End
```

A graph $G''(V, E'')$ is constructed based on the edge set E'', with G'' being a mixture of mesh and tree structures (the mixture is detailed in **Appendix B**). Fig. 3 illustrates redundant edge removal. The centers and members of three classes are labeled using squares and circles, respectively. The green edges are removed directly because of the MST in each class. The yellow edge is also removed because a clear separation must be maintained between the center of one class and the member of another class. The red edges must not be removed to ensure the connectivity of the graph. The remaining red and black edges in the figure comprise the structure of a new graph with a simplified edge set.

After applying the simplification procedure, all images in the graph must be registered iteratively along the edges in $G''(V, E'')$. The image clustering result is modified after the registrations because the differences between images have been changed. Despite maintaining the entire topology of the dataset, a fixed graph cannot be the optimal structure for accurate calculation of the atlas during the iterations. Instead of using the fixed graph, the proposed method dynamically constructs graphs during each iteration process. Given that the hidden relationships between any two images are detected in each iteration, the principal difference between the images is stored through the edges of the dynamic graph. The entire topology of the dataset is eventually preserved.

After the simplification, the local linkage of each image is strengthened. The pair images with the highest similarity are linked. According to (2), the similarity is the norm of the velocity. This indicates the scale of the deformation between the images. And the scale relates directly to the accuracy of the registration. If the scale is large, the accuracy is low; otherwise, it is high. In graph shrinkage, E'' will provide the registration patch for each image to decompose the large-scale-deformation registration into multiple registrations with small deformations. Given the small deformations, these multiple registrations estimate an accurate deformation used as an initialization of the large deformation can help the registration starting from near the global optimum and searching along the correct direction.

2.3 Weighted shrinkage

In the graph shrinkage, the deformation on the manifold between the linked images is firstly estimated using symmetric log-domain diffeomorphic (SLDD) [18] method, summarized as follows. The systematic energy function of SLDD is formulated in terms of the forward and backward energy functions $\mathrm{Energy}_{\mathrm{forw}}$ and $\mathrm{Energy}_{\mathrm{back}}$, as follows:

$$\mathrm{Energy}_{\mathrm{sys}}(I_i, I_j, s_{ij}) = \mathrm{Energy}_{\mathrm{forw}}(I_i, I_j, s_{ij}) + \mathrm{Energy}_{\mathrm{back}}(I_j, I_i, s_{ij}^{-1}) \tag{7}$$

where s_{ij} is the deformation that warps I_i to I_j, and s_{ij}^{-1} is the inverse deformation that warps I_j to I_i. The deformations s_{ij} and s_{ij}^{-1} in the image space are projected through the exponential mapping to the velocity v_{ij} on the image manifold. Therefore,

$$s_{ij} = \exp(v_{ij}) \tag{8}$$

$$s_{ij}^{-1} = \exp(-v_{ij}) \tag{9}$$

The systematic energy function can be rewritten as follows:

$$\mathrm{Energy}_{\mathrm{sys}}(I_i, I_j, v_{ij}, u^{\mathrm{forw}}, u^{\mathrm{back}}) = \mathrm{Energy}_{\mathrm{forw}}(I_i, I_j, v_{ij}, u^{\mathrm{forw}}) + \mathrm{Energy}_{\mathrm{back}}(I_j, I_i, v_{ij}^{-1}, u^{\mathrm{back}}) \tag{10}$$

where u^{forw} and u^{back} are the forward and backward update velocities, respectively. Given an initial velocity v_{ij}, $\mathrm{Energy}_{\mathrm{forw}}$ is optimized to compute the update velocities u^{forw}:

$$u^{\mathrm{forw}} = \arg\min\left(\mathrm{Energy}_{\mathrm{forw}}\right) \tag{11}$$

$\mathrm{Energy}_{\mathrm{back}}$ is optimized to compute u^{back} as (11). u^{forw} and u^{back} are then combined to update the velocity:

$$v_{ij} \leftarrow Z\left(v_{ij}, \delta v_{ij}\right) \tag{12}$$

$$\delta v_{ij} = G \otimes \left(u^{\mathrm{forw}} - u^{\mathrm{back}}\right) / 2 \tag{13}$$

where G is a Gaussian kernel and $Z(\cdot,\cdot)$ is computed through Baker-Campbell-Hausdorff (BCH) formula:

$$Z\left(v_{ij}, \delta v_{ij}\right) = v_{ij} + \delta v_{ij} + \frac{1}{2}\left[v_{ij}, \delta v_{ij}\right] + \frac{1}{12}\left[v_{ij}, \left[v_{ij}, \delta v_{ij}\right]\right] + \mathrm{O}\left(\left\|\delta v_{ij}\right\|^2\right) \tag{14}$$

$$\left[v_{ij}, \delta v_{ij}\right] = \left(\nabla v_{ij}\right)\delta v_{ij} - \left(\nabla \delta v_{ij}\right) v_{ij} \tag{15}$$

The optimal velocity field $\tilde{v}_{ij}$ is obtained through the forward and backward optimizations in each iteration. The velocity fields and corresponding deformations that deform I_i to the linked images are estimated using (12). For I_i, the deformation to warp I_i is a weighted average of the deformations between I_i and its linked images. Most existing groupwise registration methods linearly average multiple deformations with equal weights in the original image space. Consequently, this weight is the global weight for the whole deformation of I_i. A global weight for the whole deformation ignores local variation between pair images. Here, I_i is warped toward images that greatly differ from it. Dissimilar linked images might bias the overall average deformation owing to large anatomical differences that depart from the mean image at the population center of the distribution. This can considerably slow down graph shrinkage. The deformation of the whole image is not in a linear space [22]. Consequently, the global deformation which is a linear combination in the original space of images will decrease the accuracy of the groupwise registration.

To address these problems, adaptively adjusted global and local weights are proposed for the velocity during the averaging process on the image manifold.

The following rules are defined for determining the global weight w^{global}: (i) if the image is only directly connected to an image, then the global weight for the corresponding velocity is equal to one; (ii) if the image is directly connected to multiple images, then the global weights for the corresponding velocities are shared by (16) below. For instance, if I_i is connected to I_j that is one of the multiple connected images, then the global weight w_{ij}^{global} for the corresponding velocity from image I_i to I_j can be calculated as follows:

$$w_{ij}^{global} = \frac{1}{d_j} \cdot \frac{n_{ij}}{N-1}, \sum_{j=1}^{N_i} w_{ij}^{global} = 1 \tag{16}$$

where n_{ij} is the number of images in the set that is separated from all linked edges and contains I_j. $1/d_j$ is the mean factor for I_j, N is the number of the images in the dataset, and N_i is the number of connected images of I_i. The global weights are naturally normalized. Given that d_j, n_{ij} and $N-1$ are larger than zeros, the value of w_{ij}^{global} lies in the interval $(0,1]$. For the connections of I_i differing from I_j, w_{ij}^{global} might be unequal to w_{ji}^{global}.

The final atlas is located at the center of the distribution on the image manifold and approaches more images [23]. Therefore, according to (16), the warping tendency of each image can be gravitated toward its connected image set with many members in the dataset. Fig. 4 shows a simple example of global weight determination with ten images (N = 10). In this figure, three edges E''_{BA}, E''_{BC} and E''_{BD} link I_B with I_A, I_C and I_D, respectively, in a graph $G''(V,E'')$ with the simplified edge set. w^{global}_{BA}, w^{global}_{BC} and w^{global}_{BD} are the weights of the deformations on the manifold from I_B to I_A, I_C and I_D. All of the images are separated by the three edges into three image sets S_A, which contains I_A, S_B, which contains I_B, and S_{CD}, which contains the other images. Based on these sets, n_{BA}, n_{BC}, n_{BD} and the corresponding mean factors are computed. According to (16), w^{global}_{BC} is equal to w^{global}_{BD}, and is four times larger than w^{global}_{BA}. As shown in Fig. 4 (a), I_A is far away from most of other images on the image manifold, indicating that I_A greatly differs from the other images. For I_B, the distribution center on the image manifold is located closer to both I_C and I_D than to I_A. Therefore, I_B must be warped toward the direction of the connected image set that contains I_C and I_D. However, owing to the large difference between I_A and I_B, the deformation on the manifold from I_B to I_A is larger than that from I_B to I_C and that from I_B to I_D. In Fig. 4 (b), if these deformations are averaged with equal global weights, then I_B will be warped along the direction of I_A on the image manifold. The warping of I_B toward the final atlas is thereby decelerated. In contrast, in the proposed method, v_{BA}, v_{BC} and v_{BD} are averaged on the manifold with different global weights to obtain the deformation of I_B. Therefore, the deformation v_{BA} that warps I_B toward the opposite direction of the population center is weakened in the averaging.

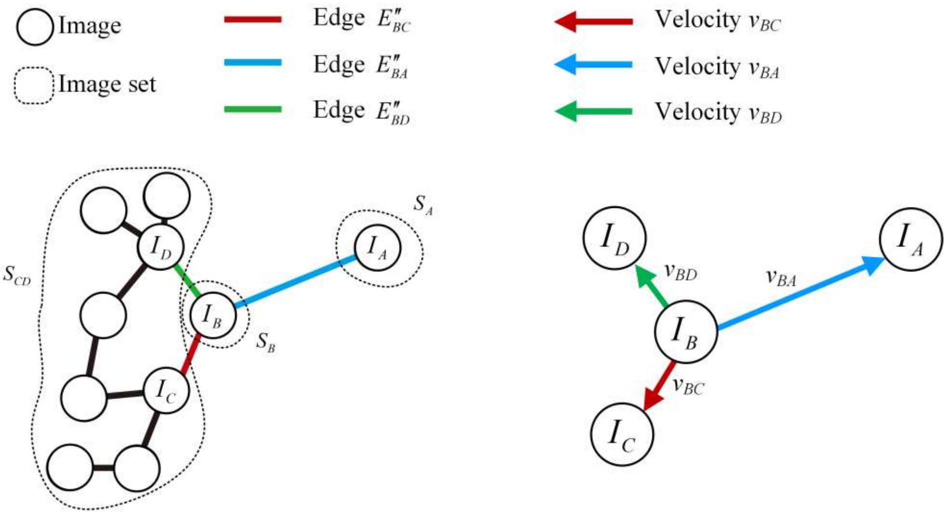

(a) (b)

Fig. 4. Determining the weights for the deformations between an image and the connected images. (a) is the connections of image I_B in the graph. (b) shows the deformations from I_B to its connected images.

The linear operation multiplying the whole deformation by the determined global weight ignores local anatomical variations. Therefore, a local weight is proposed to compensate for the global deformation in the local area. To determine local weights, key points on each class center image are extracted. The extracted key points on different class center images are different. Key points on the class members are points at the same position as those on the corresponding class center image. Patches centered at key points on the images are then extracted. The difference between the deformation of a patch and that of a whole image in a local area is used to determinate the local weight. Given that key points on the images in each class are identical, the local weight compensates only for local deformations between images of the same class. Within each class, for corresponding images I_i and I_j, the local optimal velocity between a patch P_q on I_i, and the corresponding patch P_p on I_j can be calculated using SLDD. According to (10), the systematic energy function for patches is given as follows:

$$\text{Energy}_{\text{sys}}\left(P_q, P_p, v^{patch}_{P_q,P_p}, u^{\text{forw}}_{patch}, u^{\text{back}}_{patch}\right)=\text{Energy}_{\text{forw}}\left(P_q, P_p, v^{patch}_{P_q,P_p}, u^{\text{forw}}_{patch}\right)+\text{Energy}_{\text{back}}\left(P_p, P_q, \left(v^{patch}_{P_q,P_p}\right)^{\text{-1}}, u^{\text{back}}_{patch}\right) \tag{17}$$

where $p,q \in [1,Q_i]$, Q_i is the number of key points on I_i, and $v^{patch}_{P_q,P_p}$ is the velocity at patch scale. u^{forw}_{patch} and u^{back}_{patch} are forward and backward update velocities at patch scale, respectively. The local optimal velocity $\tilde{v}^{patch}_{P_q,P_p}$ is obtained through the optimization of (17).

The weight $w^{local}_{P_q}$ at the local area of P_q is given as follows:

$$w^{local}_{P_q} = \text{NCC}\left(\tilde{v}^{patch}_{P_q,P_p}, \tilde{v}_{ij\in\Omega P_q}\right) \tag{18}$$

where $\tilde{v}_{ij\in\Omega P_q}$ is $\tilde{v}_{ij}$ for whole image in the local area of P_q. Normalization cross correlation (NCC), a metric used to evaluate the between two velocities, takes values in $[-1,1]$. Therefore, $w^{local}_{P_q} \in [-1,1]$. After computations of the weights at all local patches, we reconstruct a dense weight map $w^{rec-local}_{ij}$ for the whole velocity field based on the local weights $w^{local}_{P_q}$. Since the patches in an image might overlap, the local weights of the corresponding patches are averaged in overlap areas.

The optimal weight w_{ij} for the velocity $\tilde{v}_{ij}$ is calculated based on $w^{rec-local}_{ij}$ and w^{global}_{ij} , as follows:

$$w_{ij} = \frac{w^{global}_{ij} \cdot \left[1 + G_\sigma \otimes \left(w^{rec-local}_{ij} + \varepsilon\right)\right]}{\sum_{j=1}^{N_i} \left\{w^{global}_{ij} \cdot \left[1 + G_\sigma \otimes \left(w^{rec-local}_{ij} + \varepsilon\right)\right]\right\}} \tag{19}$$

where G_σ is a Gaussian kernel for smoothing $w^{rec-local}_{ij}$, N_i is the number of linked images and ε is a small constant. Given $w^{local}_{P_q} \in [1,-1]$, $\left(1 + G \otimes w^{rec-local}_{ij}\right)$ takes values in $[0,2]$. When w_{ij} equals to zero, the corresponding velocity $\tilde{v}_{ij}$ is not used to guide the deformation of I_i. And the edge E''_{ij} between I_i and I_j is broken which destroys the linkage of the graph G''. Therefore, ε is introduced to prevent w_{ij} from equaling to zero, thereby ensuring that $w_{ij} \in (0,1]$. Given the proposed local weight, w_{ij} is a non-linear weight for the whole image velocity. Based on w_{ij}, the velocity field v_i of I_i is a weighted average of estimated velocity fields on the manifold in each iteration and can be calculated as follows:

$$v_i = \sum_{j=1}^{N_i} w_{ij} \cdot e''_{ij} \cdot \tilde{v}_{ij} \tag{20}$$

The deformation T_i can be estimated through exponential mapping:

$$T_i = \exp(v_i) \tag{21}$$

As the step proposed in HUGS, Δt can be used to accelerate graph shrinkage and T_i can be estimated as follows:

$$T_i = \exp(\Delta t \cdot v_i) \tag{22}$$

$$\Delta t = \min\left\{ \frac{1}{\max_i \|v_i\|}, \frac{\sum_{i,j=1}^{N} e''_{ij} w_{ij} \left\|\tilde{v}_{ij}(k)\right\|^2}{2\sum_{i,j=1}^{N} e''_{ij} w_{ij}^2 \left\|\tilde{v}_{ij}(k)\right\|^2} \right\} \tag{23}$$

Images in the data set will be warped to the final atlas with the weight obtained in each iteration. The differences between the images decrease with the magnitude of the image warping. To monitor these difference, an energy function of the groupwise registration is constructed as follows:

$$\text{Groupwise-Energy}= \sum_{i,j=1}^{N} e''_{ij} d\left(I_i, I_j\right)^2 = \sum_{i,j=1}^{N} e''_{ij} \left\|\tilde{v}_{ij}\right\|^2 \tag{24}$$

The derivative of the groupwise energy is as follows:

$$div\left(\text{Groupwise-Energy}\right) = -4\left(\sum_{i.j=1}^{N} e''_{ij} w_{ij} \left(1 - w_{ij}\right) \left\|\tilde{v}_{ij}(k)\right\|^2 \right) \tag{25}$$

Given $w_{ij} \in \left(0,1\right]$, this derivative is negative (The proof is detailed in **Appendix C**). Therefore, throughout weighted graph shrinkage, the groupwise energy decreases, and all images are warped to a convergent atlas.

3. Experiment and Discussion

The proposed groupwise registration method is evaluated using synthetic and clinical datasets. The normalized mutual information (NMI), the mean squared difference (MSD) and the Hausdorff distance (HDD) are taken as evaluation criteria to assess the registration accuracy of the proposed method. The synthetic dataset of Jia et al. [9] is used to assess the proposed method, which is also compared with other existing methods, including Group-mean [10], GWMI [13], DDG [14], ABSORB [9], SharpMean [12] and HUGS [16]. The proposed method is compared with Group-mean, GWMI, ABSORB and SharpMean methods to examine the advantages of the graph-based framework without a template at the bias of the resultant atlas. Furthermore, the proposed method is compared with DDG and HUGS methods to examine the advantages of using the local distribution at the rapid groupwise registration. For the proposed method, the graph shrinkages with global and global+local weight are also compared to examine the advantages of using the local compensation for the whole deformation at the accuracy of the resultant atlas. The proposed method is then examined to demonstrate its accuracy and efficiency in registering clinical liver CT images obtained from the SLIVER 2007 MICCAI Grand Challenge Workshop [24]. A liver probabilistic atlas (LPA) is constructed by the proposed method. The histogram entropy is used to evaluate fuzziness of the atlas:

$$EN = -\sum_{i=1}^{N_{bin}} pb_i \log\left(pb_i\right) \tag{26}$$

$$pb_i = \frac{NM(b_i)}{\text{sum}(NM(b_i))} \tag{27}$$

where b_i and $NM(\cdot)$ denote the i^{th} histogram bin and corresponding voxel number, respectively. Here, N_{bin} denotes the number of bins used in the histogram. In the foreground of LPA, the intensity range is $\left(0,1\right]$. If the intensities of all voxels in the foreground are equal to one, so the corresponding probability pb is equal to one, and the boundary of this atlas is sharp. According to (26), the histogram entropy of this atlas is equal to zero. Therefore, if the result of (26) approaches zero, the boundary of the atlas is sharp; otherwise is blurred.

A mean shape model can be extracted from LPA. The dice similarity coefficient (DSC) is taken as the accuracy measure of the extracted mean shape model. DSC is computed as follows to measure the overlap degree between the regions of two arbitrary images I_i and I_j :

$$\mathrm{DSC} = \frac{2 \cdot Num(I_i \cap I_j)}{Num(I_i) + Num(I_j)} \tag{28}$$

where $Num(\cdot)$ is the regional voxel number. The accuracy of the model is measured by computing the DSC between the mean shape model and the warped images after groupwise registration.

3.1 Evaluation for synthetic dataset

As shown in Fig. 5, the synthetic dataset consists of 61 (20×3+1) two-dimensional (2D) images which are distributed in three branches, each branch (with 20 images) is generated from the same base image. Therefore, the base image is the original undistorted image and the ground truth. The size of each image is 256×256. There are two labels, viz. 64 and 128, representing the different tissues in the foreground of these images. The background intensity is zero. The baseline image in this dataset represents the ground truth, which is deformed to generate images of three types. Group-mean, GWMI, DDG, ABSORB, SharpMean, HUGS, and the proposed method are all used to construct the atlas using the synthetic dataset. To examine the advantages of the global+local weighting for the proposed method, graph shrinkage with global and global+local weights are tested, respectively.

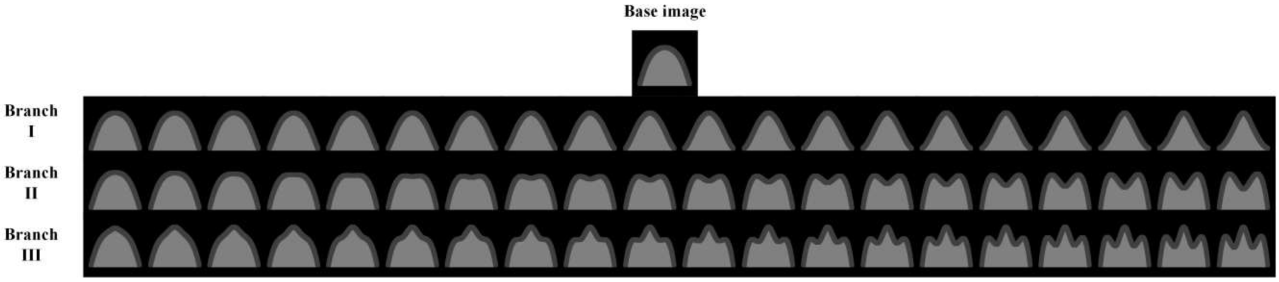

Fig. 5. Simulated dataset

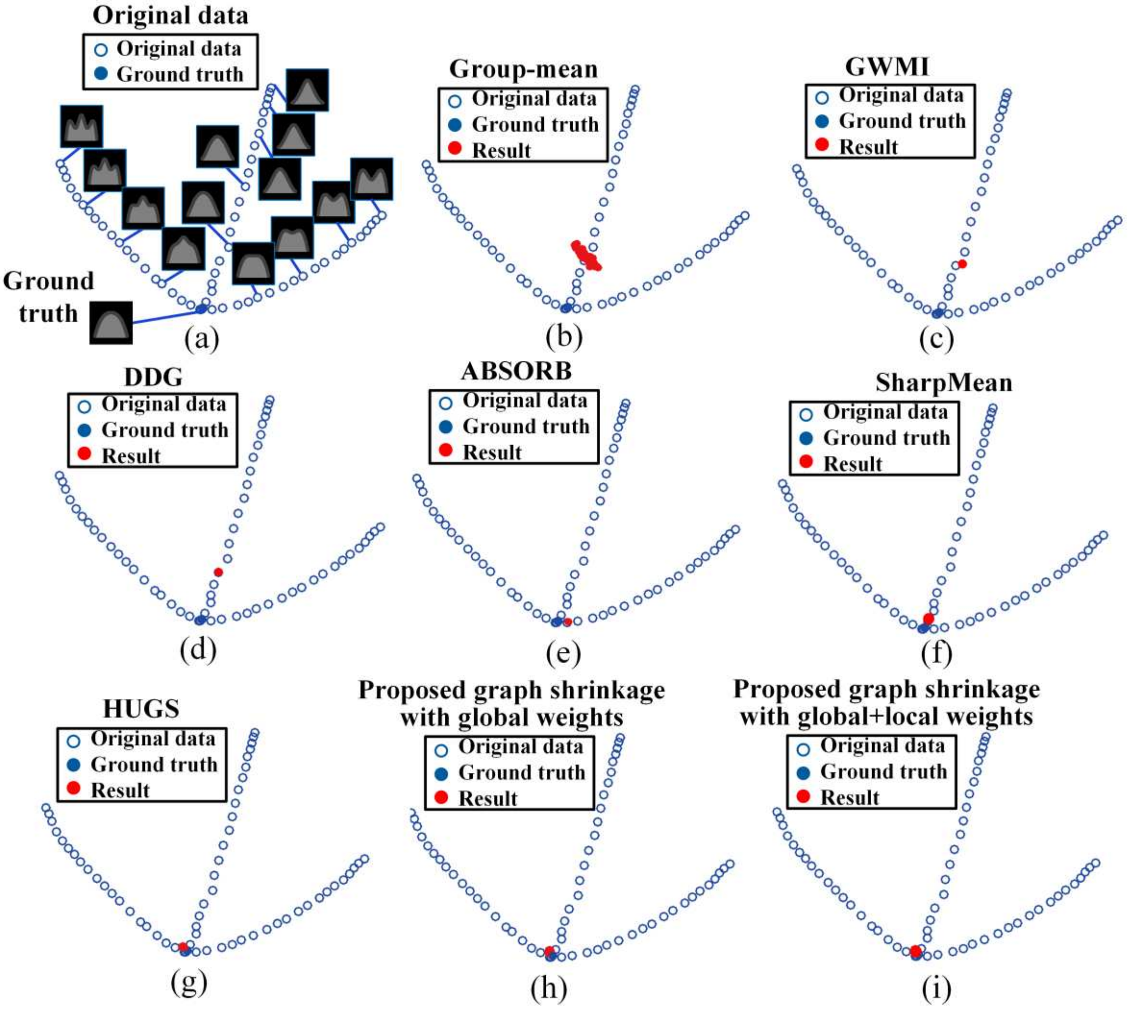

Fig. 6. Distribution of the synthetic dataset and warped images in the projected 2D space. (a) shows the original dataset. (b-g) show the results of Group-mean, GWMI, DDG, ABSORB, SharpMean, and HUGS, respectively. (h) and (i) show the results of the proposed graph shrinkage with global and global+local weights, respectively.

To illustrate the shrinkage process, all original and warped images obtained through the registration are projected to a 2D space using principal component analysis (PCA) as shown in Fig. 6. In Figs. 6 (a) through (j), the blue circles represent the original data, the solid blue dot represents the ground truth, and the solid red dots represent the warped images. Fig. 6 (a) shows the 2D distribution of the original dataset, while Figs. 6 (b) through (g) show the final registration results of Group-mean, GWMI, DDG, ABSORB, SharpMean, and HUGS. Figs. 6 (h) and (i) show the results of the proposed graph shrinkage with the global and global+local weights, respectively.

Based on the projection results of PCA, the distance between the red and blue solid dots in Fig. 6 represents the similarity between the final atlas and the ground truth. The shorter distance denotes the higher similarity. For Group-mean, as shown in Fig. 6 (b), the local differences between image types result in blurring of the initial mean image. The registration accuracy of Group-mean decreases considerably because of the fuzziness of the initial mean image. Given that the differences between the warped images are not small, these images do not converge to an image that is a point in a 2D space. The groupwise mutual information is used to select an image in the dataset as an initial sharp template image in GWMI. Through mean deformation, the initial template image is warped to the final atlas with high resolution as indicated by a red dot in the 2D space in Fig. 6 (c). In contrast to GWMI, DDG method uses the dynamic directed graph to guide the groupwise registration of images. These images are registered to their parent images along the edges toward the final atlas, and the accuracy of the registration from the image to the final atlas is improved through the parent image. The warped images converge to a red dot in Fig. 6 (d), resulting in a high-resolution atlas. Although GWMI and DDG result in high-resolution atlases, the red dot is far away from the blue solid dot in the 2D space. Therefore, given the bias in selecting the initial mean image, a large difference is observed between the resultant atlas and the ground truth. ABSORB selects the median image on the learned manifold as a template, while SharpMean uses the adaptive weights to estimate a template. Therefore, the projected final atlases of these methods are closer to the ground truth than that of Group-mean, GWMI, and DDG in the 2D space in Figs. 6 (e) and (f). However, since a template image must be selected to initiate groupwise registration, a potential bias inevitably exists in the final atlases of ABSORB and SharpMean. Fig. 6 (g) shows that HUGS can obtain a relatively accurate result using the unpruned edges in the graph to guide the groupwise registration. Figs. 6 (h) and (i) compare the result of the proposed graph shrinkage with the global and global+local weights. The differences between the warped images are small and these images are close to the ground truth.

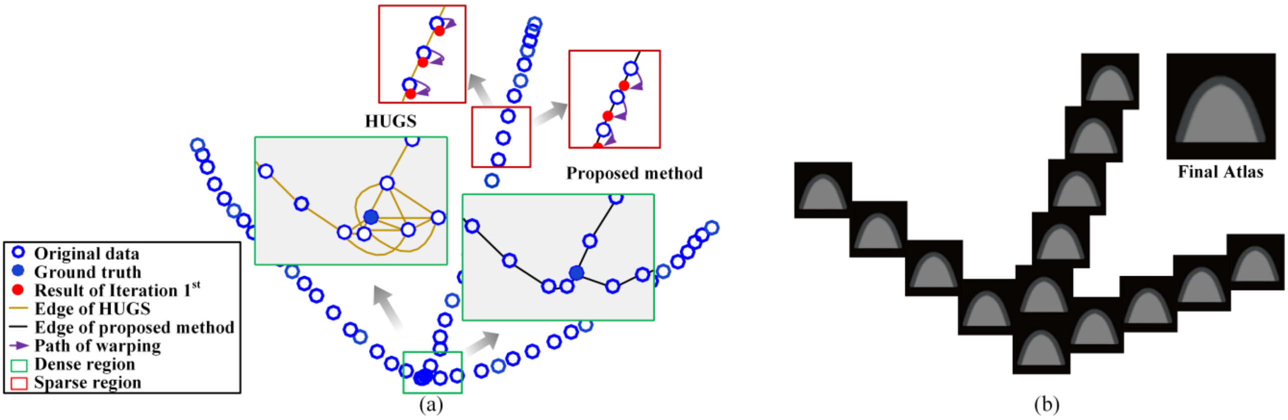

(a)

(b)

Fig. 7. Results of the synthetic dataset. (a) illustrates the edges and the results of the proposed method and HUGS in the first iteration. (b) illustrates the result of the proposed method.

Given the similar results in the 2D space, a further comparison is performed to reveal the underlying differences between HUGS and the proposed method. Fig. 7 (a) shows the registration results of HUGS and the proposed method after the first iteration. The blue circles represent the original data, the solid blue dot represents the ground truth, and the solid red dots represent the warped images after the first iteration. The green regions contain the images in the dense distribution on the image manifold. The yellow and black lines indicate the edges of the graphs using HUGS and the proposed method, respectively. The redundant edges are included in the groupwise registration using HUGS. Hence, this method is very time-consuming. The proposed method uses a simplified edge set to detect the hidden relationship between two images, decreasing the number of edges. The red regions contain those images in the sparse distribution on the image manifold, and both methods show the similar edges. In these regions, the warping paths produced by the proposed method show larger displacements from the original images to the ground truth than those estimated by HUGS. These large displacements indicate that the allocation of dynamic weight increases the convergence speed. By incorporating the simplified edge set and dynamic weights, the proposed method not only maintains the accuracy level but also shrinks the graph at an increased speed. The resultant images of those sampled in Fig. 6 (a) are collected in Fig. 7 (b) to portray the effects of iterative registration using the proposed method. The warped images are almost identical and the final atlas is highly similar to the ground truth, as shown in the upper right of Fig. 7 (b).

TABLE I

Required time, MSD, mean DSC and mean HDD of the different methods

	Group-mean	GWMI	DDG	ABSORB	SharpMean	HUGS	Proposed graph shrinkage with global weights	Proposed graph shrinkage with global+local weights
MSD	307.1	110.3	162.6	70.5	93.2	70.0	24.5	20.1
Mean DSC_{64} (%)	54.2	82.3	81.6	93.5	90.9	91.8	94.4	95.1
Mean DSC_{128} (%)	74.7	86.8	83.1	92.6	90.1	93.5	95.2	96.7
Mean HDD_{64} (pixel)	12	3	5	3	2	1	1	1
Mean HDD_{128} (pixel)	11	4	5	2	2	2	1	1
Time (hour)	3.1	4.4	16.3	10.5	5.1	23.8	13.2	17.8

In Table I, three metrics are computed to evaluate the registration accuracy of different methods. MSD between the intensities of the ground truth and the final atlases are presented in the second line. Given the two tissues with the labels, viz. 68 and 128, in the foreground of the synthetic images, the final atlases are segmented by thresholding to obtain the labels of these two tissues. The mean DSC and HDD for each tissue between the labels of 61 warped images and the final atlases are computed. The mean DSC_{64}, mean DSC_{128}, mean HDD_{64} and mean HDD_{128} represent the corresponding values of DSC and HDD for the two tissues, respectively. To examine the advantages of the global+local weighting, the last two columns compare the registration accuracy of the proposed graph shrinkage with global weights and that with global+local weights. The small MSD and HDD and high DSC indicate a highly accurate registration result. Therefore, the proposed framework obtains a result more accurate than those of the other methods. Meanwhile, the proposed graph shrinkage with global+local weights achieves more accurate result than that obtained with global weights. This table also compares the time requirements of these methods. Since that the patch-wise registrations are used to compute the local weight, the proposed graph shrinkage with global+local weights consumes more time than that with global weights. The proposed method shrinks a graph with a simplified edge set rather than with the superfluous edge set link used in HUGS. Therefore, HUGS consumes more time than the proposed method.

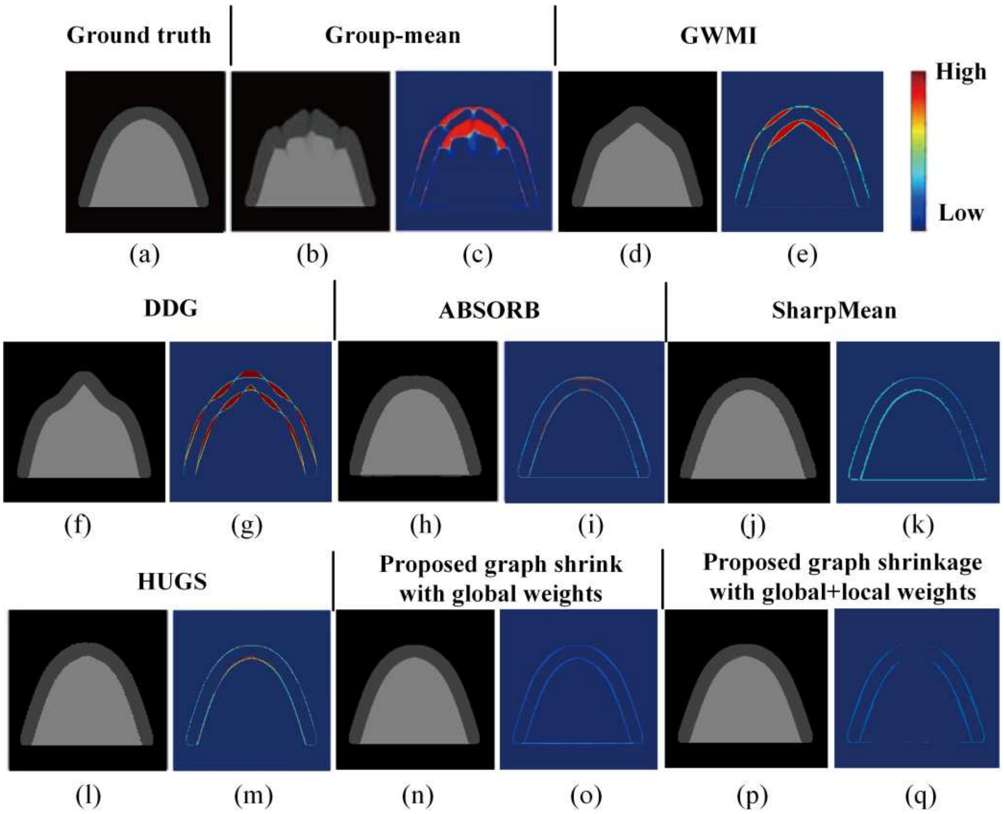

Fig. 8. Registration results and the corresponding comparisons with the ground truth. (a) shows the ground truth. (b), (d), (f), (h), (j), (l), (n) and (p) present the final atlases obtained by Group-mean, GWMI, DDG, ABSORB, SharpMean, HUGS, the proposed graph shrinkage with global weights and that with global+local weights, respectively. (c), (e), (g), (i), (k), (m), (o) and (q) show the corresponding error images.

The graphical illustrations of the registration error measures are paired with the final atlases obtained by each method, and these atlases are then lined up with the ground truth in Fig. 8. Fig. 8 (a) shows the ground truth, Figs. 8 (b), (d), (f), (h), (j), (l), (n) and (p) show the results of Group-mean, GWMI, DDG, ABSORB, SharpMean, HUGS, the global+local with global weights and global+local weights, respectively, and Figs. 8 (c), (e), (g), (i), (k), (m), (o) and (q) show the corresponding error images. The warm and cold colors in these error images signify large and small errors, respectively. For the groupwise registration with the mean image as the template, the large area with the warm color in Fig. 8 (c) indicates a large error in the final atlas of Group-mean with the blurred mean images. For the groupwise registration with the selected image as a template, the biases in the selection introduce the error in the final atlas of GWMI and DDG in Figs. 8 (e) and (g). The areas with warm colors are reduced by using ABSORB and SharpMean with a sharp template that is close to the ground truth in Figs. 8 (i) and (k). HUGS and the proposed method use the graph to guide the groupwise registrations without a template. However, the unpruned edges in the graph used in HUGS decreases the accuracy of the result. Therefore, the proposed framework produces thinner error stripes around the margin than HUGS, particularly at the top of the atlas in Figs. 8 (m), (o) and (q). Meanwhile, the error of the atlas obtained by the proposed graph shrinkage with global+local weights is smaller in the local area than that with global weights. On the trade-off between computational time and accuracy, the proposed graph shrinkage with global+local weights obtains the most accurate result with the least computational demand.

3.2 Evaluation for clinical dataset

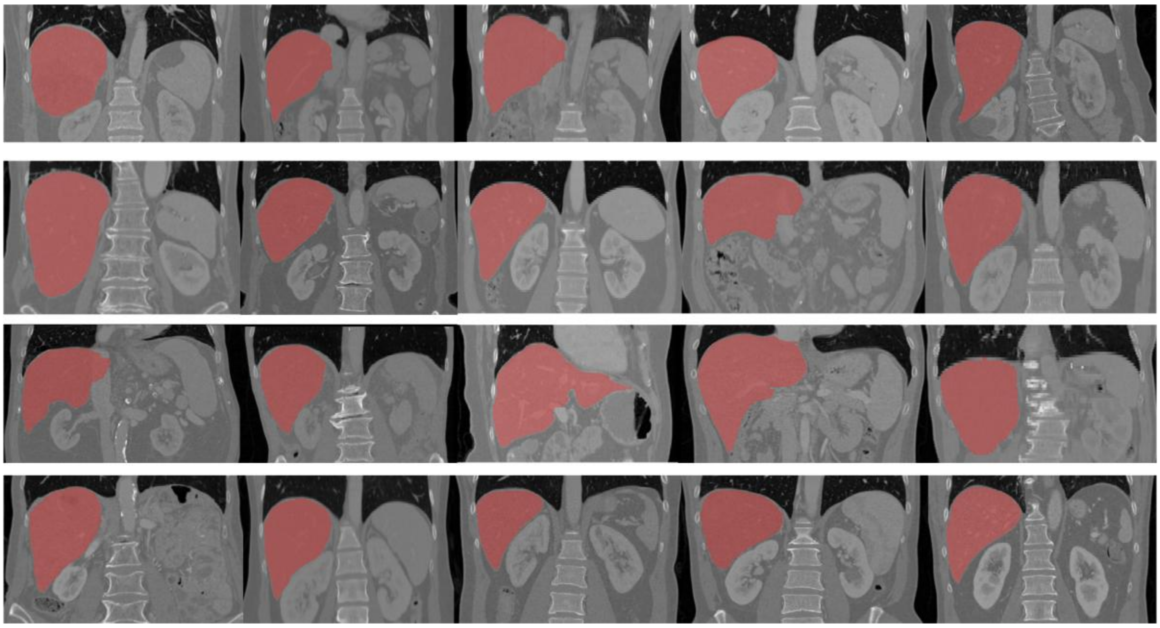

Fig. 9. 20 Clinical CT images with the liver segmentation (red area).

As shown in Fig. 9, a collection of 20 clinical liver computed tomography (CT) images with segmentation results, in which large anatomical differences can be identified, is used for evaluation. Each image has different sizes and voxel resolutions. To achieve groupwise registration, each image in the dataset is affine aligned to the first image using the iterative closest point, a point cloud registration method [25]. All images are resampled and normalized to an identical size of 256 × 256 × 100 and voxel resolution of 1.48 mm × 1.48 mm × 1.00 mm.

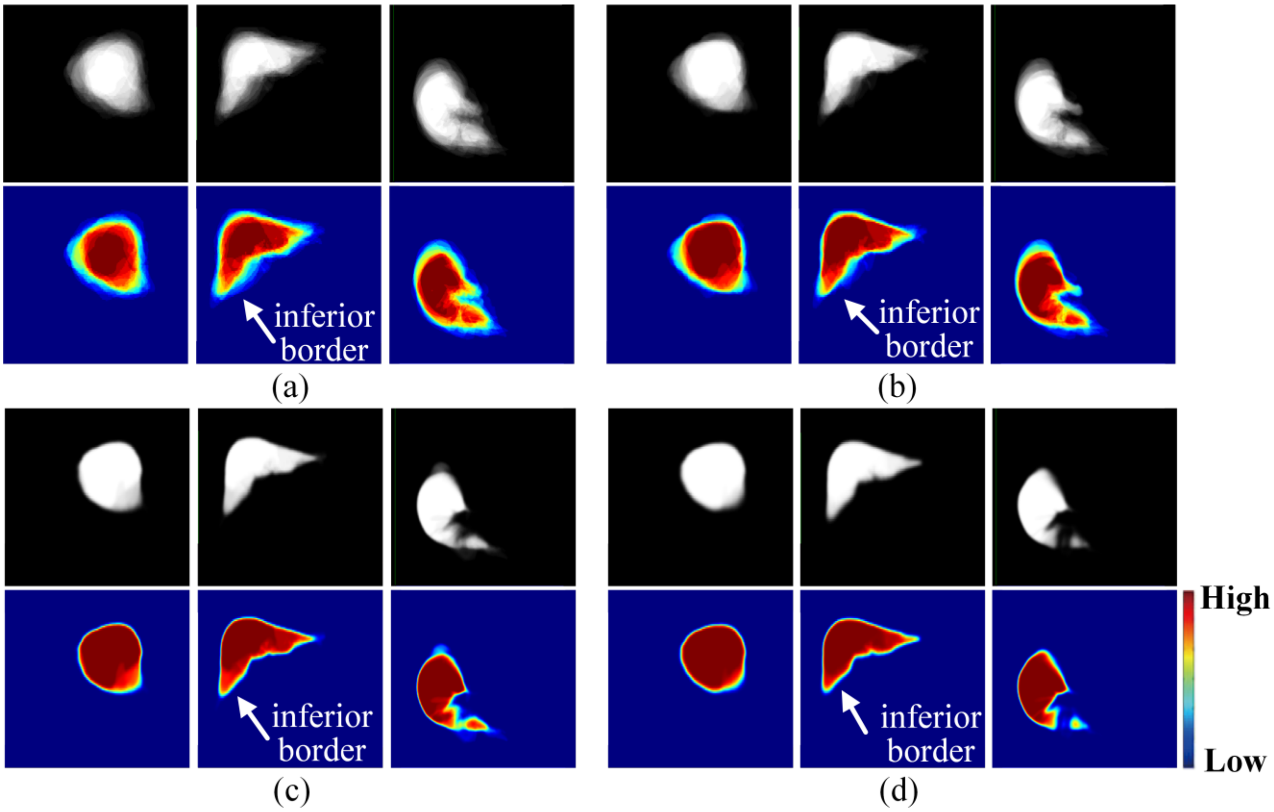

Fig. 10. Registration results in the different iteration. (a) shows the initial mean image. (b) and (c) show the intermediate images in the registration process using the proposed method. (d) shows the final registration result of the proposed method.

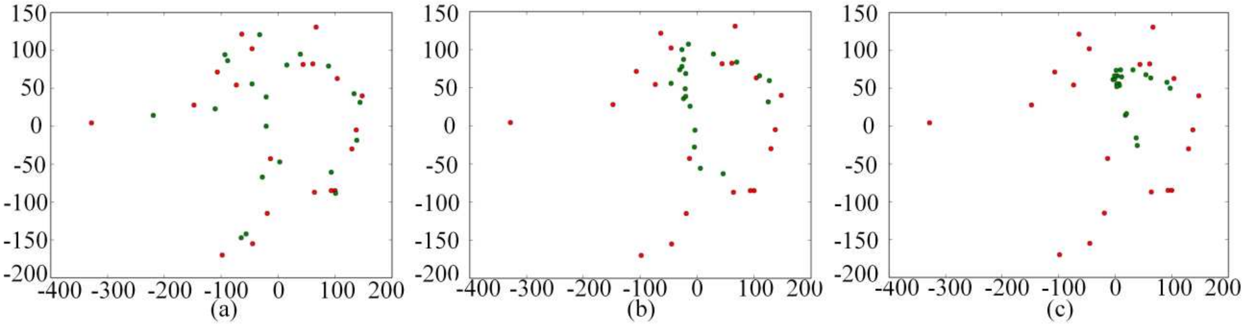

Fig. 11. Registration process and results projected in a 2D space using PCA. (a) and (b) present the intermediate processes using the proposed method. (c) shows the final registration result using the proposed method.

The affine-aligned images are warped to construct an atlas using the proposed algorithm. The initial mean image of the segmentation results in the input dataset, and the resultant mean images after the graph shrinkage at the end of the first, fifth, and ninth iterations are shown in Fig. 10 with their corresponding sagittal, coronal, and axial cross sections. The first and third rows of the figure show the mean images with intensities ranging from zero to one. An intensity close to one indicates a high similarity among the warped images. The more areas with intensities equal to one, the greater sharpness the mean image can reach. Figs. 10 (a) through (d) show the process of the mean images varying from fuzzy to sharp through iterations. The second and fourth rows of Fig. 10 show the color spectra that represent the sharpness of the corresponding mean images. The colors blue and red represent the lowest and highest intensities of the mean image, respectively. A redder spectrum indicates a higher similarity among the warped images. Figs. 10 (a) through (d) show that the colored margin of the liver measures the differences in the shapes of the warped images and represents the sharpness of the mean image. The margin of the liver in the initial mean image is blurry. Through iterations, the blurred regions are gradually reduced and the margin of the liver is sharpened, especially in the inferior border of the liver. The inner liver area with higher similarity colored dark red continues to expand through iterations and becomes the largest after the ninth iteration. Therefore, the resultant mean image can be the final liver probabilistic atlas.

Fig. 11 further evaluates the results of the proposed algorithm. The original and warped liver images are projected in the 2D space using PCA to illustrate the groupwise registration process. The original liver images are marked in red dots, while the warped images at the first, fifth, and ninth iterations are marked in green dots. The green dots in Figs. 11 (a) through (c) converge toward the final atlas in a 2D space. Given the dynamic weight allocation, all images are gravitated toward the connected sets with a larger number of members. Therefore, no zigzag path is observed during graph shrinkage.

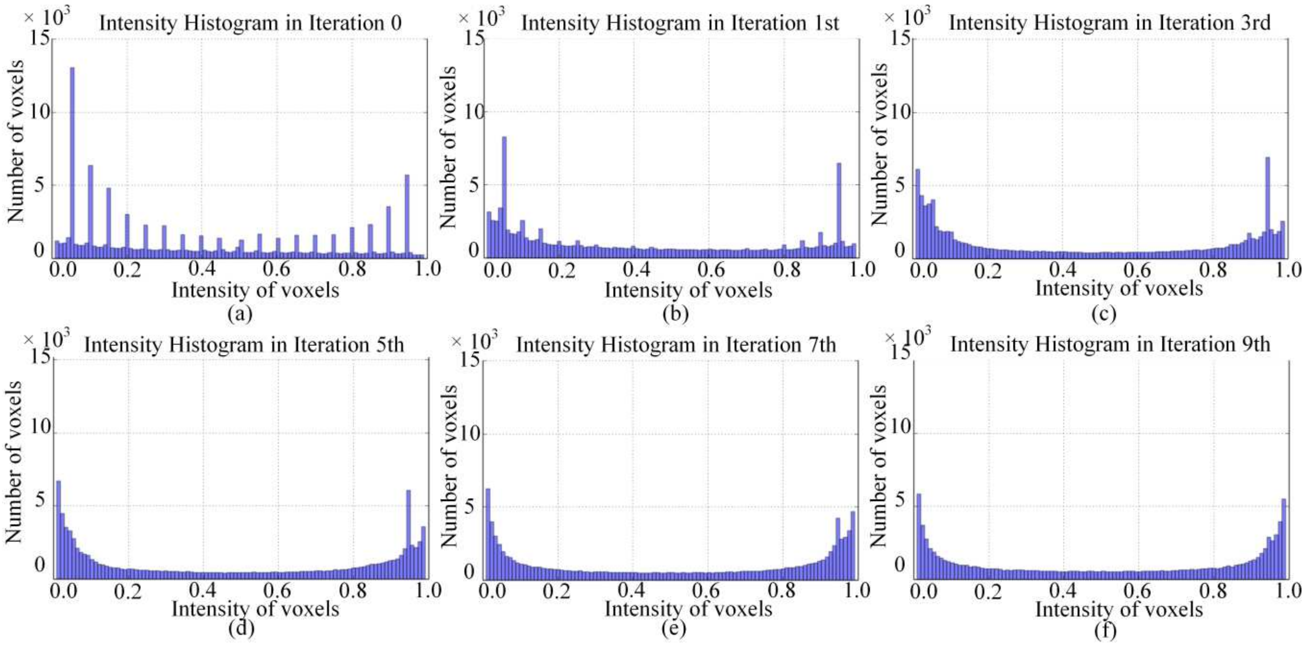

Fig. 12. Intensity histogram of the mean images before and after the proposed groupwise registration.

TABLE II

Number of edges before and after the simplification in the proposed groupwise registration through iterations

Iteration	1	2	3	4	5	6	7	8	9
E	62	88	76	74	86	98	90	100	92
E'	46	60	48	45	56	58	50	62	53
E''	41	51	43	41	48	50	46	56	49

Fig. 12 shows the histograms of the mean images of the liver segmentation before and after the proposed groupwise registration. The range of the included voxel intensity values is (0,1), and 100 bins in total are used ($N_{bin} = 100$). Before the groupwise registration process, most intensities of the liver in the initial mean image are close to zero and the distribution is cluttered, leading to the unsharp margin of the liver in the mean image. Given the large differences among the livers unregistered to the common space, the histogram of the initial mean image shows many peaks. These peaks reflect the anatomical variability across individual livers. However, after groupwise registration using the proposed method, the intensities are separated and clustered around zero and one, indicating a binary distribution. Here, the liver in the mean image has sharper contours. Using (26), the histogram entropy decreases from 0.946 to 0.523 as shown in Fig. 13 (a). The decreased entropy indicates that the intensity distribution is close to a binary distribution and that the liver boundaries are sharpened.

To demonstrate the advantages of the graph with the simplified edge set, Table II compares the number of edges before and after the simplification of the superfluous inter- and intraclass edges as function of the number of iterations in the proposed method. The number of edges in the set E before simplification is shown in the second row of Table II. The superfluous inter- and intraclass edges are deleted by the method in *edge simplification*. The corresponding simplified edge sets are E' and E'', respectively. The numbers of edges in these two sets appear in the third and fourth rows of Table II. After simplification, the edges in the dynamic graph reduce in number with use of the proposed method. A larger number edges in the graph corresponds to a larger number of required registrations between images. Therefore, the computation time associated with individual registrations increases considerably. The proposed method removes redundant edges. A lower number of edges corresponds a more marked reduction in registration time and accumulated registration errors. Since the similarities between the images increase with iterations, the number of clusters decreases from five to three. The number of clusters will affect the result of the edges simplification. Fig. 13 (b) shows the number of intra- (black line) and interclass (red line) superfluous edges in each iteration. A greater number of images in a class corresponds to more intraclass superfluous edges in the graph. Therefore, an increased number of images in each class results in an increased number of intraclass superfluous edges as the number of clusters decreases. Given the separation between the center of one class and the member of another class, the number of interclass superfluous edges is always small.

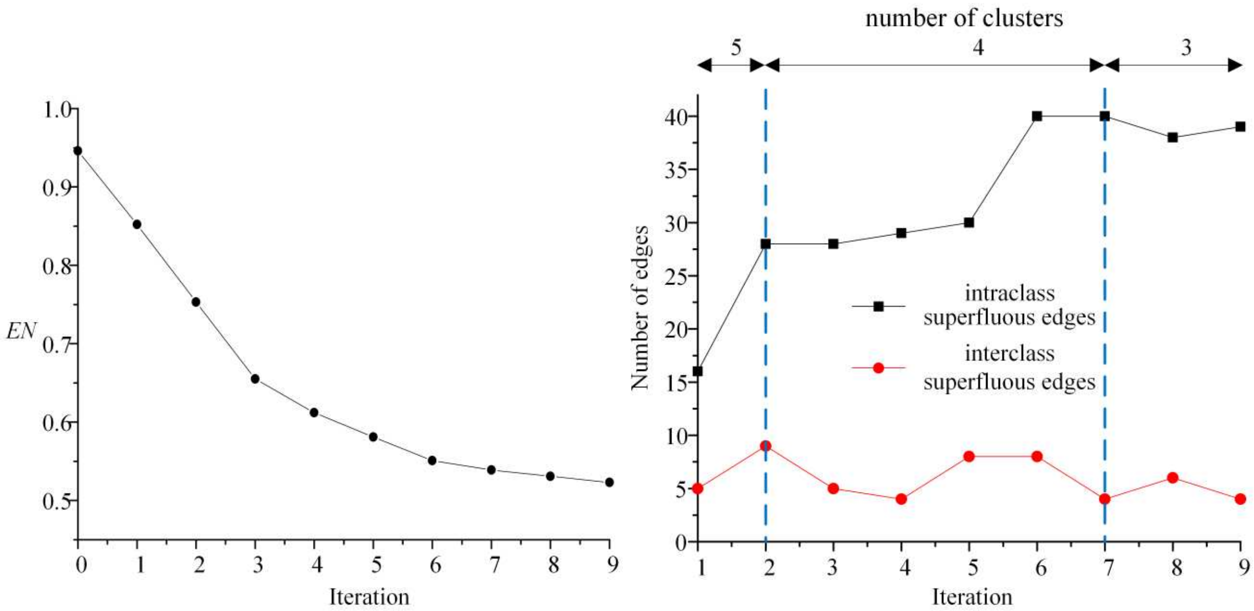

Fig. 13. Histogram entropy (a) and number of intra- and interclass superfluous edges (b) in each iteration.

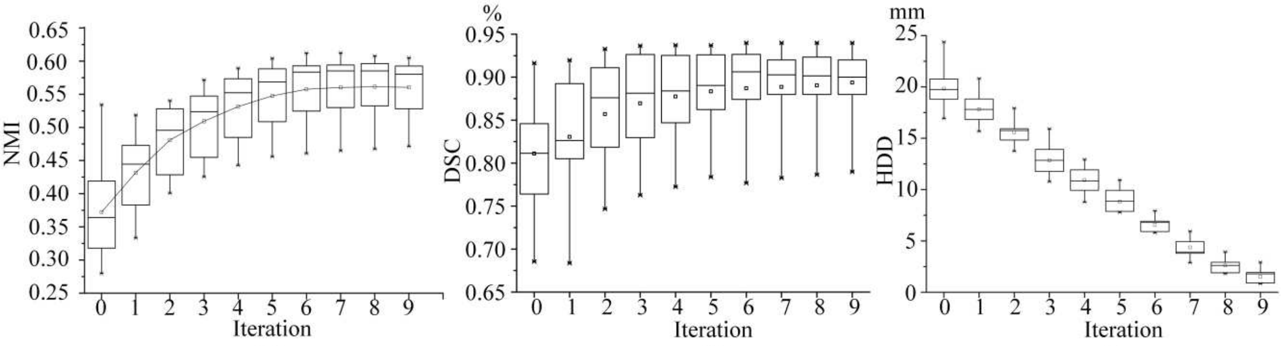

(a) (b) (c)

Fig. 14. Evolution of the NMI, DSC and HDD during the groupwise registration using the proposed method.

For the obtained LPA, the intensity of each voxel reflects the probability that the voxel belongs to the liver. Therefore, a mean shape model can be extracted from the LPA by determining the threshold during pre-surgical analysis [26, 27]; this model can also be used as an intermediate template for pairwise registration [28, 29]. The threshold for the proposed method is adaptively determined based on similarities between the warped and mean images. NMI values between the 20 wrapped images and the mean image are shown in Fig. 14 (a). As shown in this figure, the dispersion in the similarities decreases through the iterations, indicating that the proposed method effectively decreases the differences across the images. The curve in this figure indicates that the mean NMI value increases. This mean NMI value is treated as the threshold at each iteration to segment liver from the mean image. The DSC and HDD between livers in the mean and warped images are calculated and shown in Figs. 14 (b) and (c), respectively. The DSC ratio gradually increases and the HDD gradually decreases with each iteration, indicating that the livers in the warped images converge to the mean liver and the similarities between them gradually increase. The variances of the DSC ratio and HDD also decrease as the number of iterations grows, showing a higher consistency of the registration results across the whole dataset.

Fig. 15 shows the liver segmentation in the mean image at each iteration. Given the large differences among the original images, the initial liver segmentations demonstrate the roughness on the surface in Fig. 15 (a). The bumpy surface of the initial liver segmentation becomes smooth through iterations. In the ninth iteration, the similarities between the livers in the warped images are large, and the segmentation of the labeled liver is smooth. Therefore, this segmentation in the ninth iteration is a mean shape liver model. This mean shape model based on the proposed groupwise registration of a full liver dataset is a favorable average representation of liver shape.

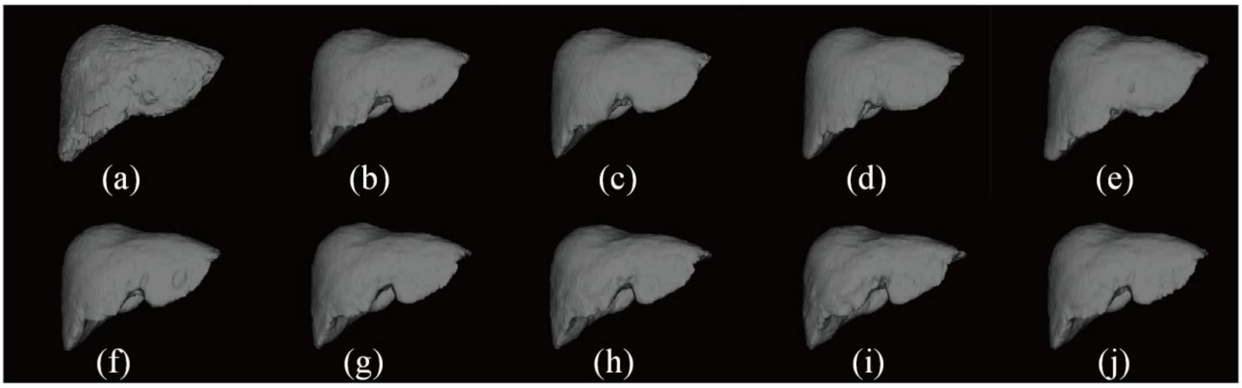

Fig. 15. Results of the shape model with the threshold. (a) Presents the result of original data, (b) to (j) show results of the first to ninth iterations, respectively.

4. Conclusion

This paper proposes a groupwise registration with global-local graph shrinkage in atlas construction. Local distributions of the dataset and local variations between the paired images are used to make the proposed graph shrinkage simplified and accurate. The proposed method is applied on synthetic and clinical datasets to evaluate its atlas construction performance. The experimental results of the proposed method are compared against those of Group-mean, GWMI, DDG, ABSORB, SharpMean and HUGS. The proposed method shows the least bias in graph shrinkage when applied on the synthetic dataset. The proposed method is also suitable for those datasets with different distributions. The graph constructed by the proposed method shows fewer number of edges, which reduces the error resulting from the larger number of registrations in the area with denser image distribution. The images in the area with sparse distribution are guided by weights and warped more rapidly toward a final atlas. Standard deviation, histogram entropy, NMI, MSD and DSC are used to evaluate the performance of the proposed method in the clinical dataset. Evaluation results indicate that our approach generates an accurate atlas efficiently.

5. Acknowledgments

This work was supported by the National Key R&D Program of China (2017YFC0112000), and the National Science Foundation Program of China (61672099, 81627803, 61501030, 61527827). AFF was partially funded by the Engineering and Physical Sciences Research Council (EP/N026993/1), the Royal Society International Exchanges Program (IE141258), and the European Commission (H2020-SC1-PM-16-2017-777119).

6. Appendix

Appendix A. Example of the Fuzzy Clustering for the Optimal Threshold Computation

An example is given in this appendix to illustrate the process of the fuzzy clustering in the proposed method. Giving a symmetric similarity matrix **R** for a set of 7 images as:

$$\mathbf{R}=\begin{bmatrix} 1 & & & & & & \\ 0 & 1 & & & & & \\ 0.1 & 0 & 1 & & & & \\ 0 & 0.9 & 0.7 & 1 & & & \\ 0.8 & 0 & 0.6 & 0 & 1 & & \\ 0.9 & 0.8 & 0 & 0.9 & 0.7 & 1 & \\ 0.6 & 0.9 & 0.1 & 0 & 0.5 & 0.4 & 1 \end{bmatrix} \tag{A.1}$$

Then, $\mathbf{R}^2$, $\mathbf{R}^4$ and $\mathbf{R}^8$ are computed by the max-min composed operation. Then, $\mathbf{R}^4$ is equal to $\mathbf{R}^8$:

$$\begin{aligned}\mathbf{R}^8 &= \mathbf{R}^4 = \mathbf{R}^2 \circ \mathbf{R}^2 = (\mathbf{R}\circ\mathbf{R})\circ(\mathbf{R}\circ\mathbf{R}) \\ &= \begin{bmatrix} 1 & & & & & & \\ 0.9 & 1 & & & & & \\ 0.7 & 0.7 & 1 & & & & \\ 0.9 & 0.9 & 0.7 & 1 & & & \\ 0.8 & 0.8 & 0.7 & 0.8 & 1 & & \\ 0.9 & 0.9 & 0.7 & 0.9 & 0.8 & 1 & \\ 0.9 & 0.9 & 0.7 & 0.9 & 0.8 & 0.9 & 1 \end{bmatrix}\end{aligned} \tag{A.2}$$

The minimum transitive closure matrix $t(\mathbf{R})=\mathbf{R}^4$. Through the max-min composed operation, the values in the matrix become larger, and the number of the different values become fewer. There are four non-zero values in $t(\mathbf{R})$, and we have $\hat{H}_q, q=1,2,3,4$, where $\hat{H}_1=1$, $\hat{H}_2=0.9$, $\hat{H}_3=0.8$, $\hat{H}_4=0.7$. The different thresholds $th\in[0,1]$ are chosen to cluster the images. If $t(\mathbf{R})_{ij}$ $(i,j\in[1,7])$ is bigger than the threshold, images I_i and I_j are clustered in the same class. Fig. A1 illustrates the process of the fuzzy cluster. The range of the threshold is divided into four parts: $th\in[1,0.9)$, $th\in[0.9,0.8)$, $th\in[0.8,0.7)$, and $th\in[0.7,0]$. When the threshold is chosen in $[1,0.9)$, the clustering result $\{I_1\}\cup\{I_2\}\cup\{I_3\}\cup\{I_4\}\cup\{I_5\}\cup\{I_6\}\cup\{I_7\}$ is obtained. Here, $\{.\}$ represents that the images in it belong to the same class. When the threshold is chosen in $[0.9,0.8)$, the clustering result $\{I_1,I_2,I_4,I_6,I_7\}\cup\{I_5\}\cup\{I_3\}$ is obtained. When the threshold is chosen in $[0.8,0.7)$, the clustering result

$\{I_1, I_2, I_4, I_5, I_6, I_7\} \cup \{I_3\}$ is obtained. When the threshold is chosen in $[0.7, 0]$, all the images are clustered into the same class as $\{I_1, I_2, I_3, I_4, I_5, I_6, I_7\}$. These results suggest that $\min(\hat{H}_q) = 0.7$ can cluster all the images into a class, so all the images are linked. Meanwhile, $\min(\hat{H}_q)$ is the maximum threshold in the range that clusters all the images into a class, so the number of the filtered edges by $\min(\hat{H}_q)$ is minimal. So, the edge set filtered by $\min(\hat{H}_q)$ satisfies *Conditions 1* and *2,* and $\min(\hat{H}_q)$ is the optimal *H*. In the graph construction, if $R_{ij} \geq \min\left(\hat{H}_q\right)$, images I_i and I_j are linked with edge. Fig. A2 illustrates the constructed graphs by different thresholds, where Fig. A2(c) is the graph with the optimal threshold.

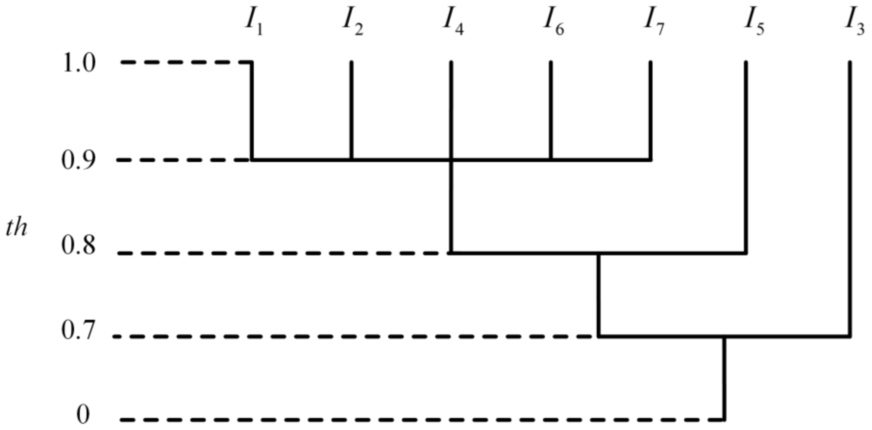

Fig. A1. The process of the fuzzy cluster

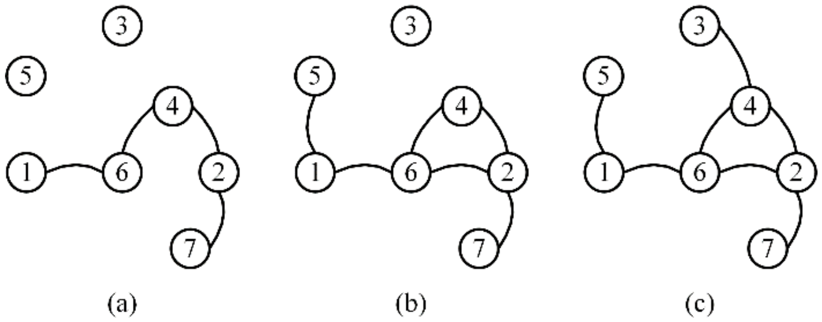

Fig. A2. The constructed graphs by different thresholds. (a) threshold is 0.9, (b) threshold is 0.8, (c) threshold is 0.7.

Appendix B. The Mixture Structure of the Simplified Graph

After the simplification of the edge set, the graph is a mixture of the mesh and the tree structures. Tree is the structure of a connected graph without cycles. In graph theory, cycle is a path starting and ending on the same node in Fig. B1. Therefore, any two nodes are connected by one path in the tree structure. Mesh is the structure of a connected graph in which each node is linked with more than two edges. And the cycle exists in the mesh structure.

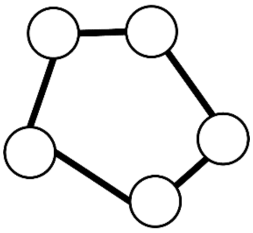

Fig. B1. Example of the cycle

In each class, MST is introduced to simplify the intraclass redundant edges. Based on the graph displayed in Fig. 2, Fig. B2 shows the structures in different classes before and after simplification.

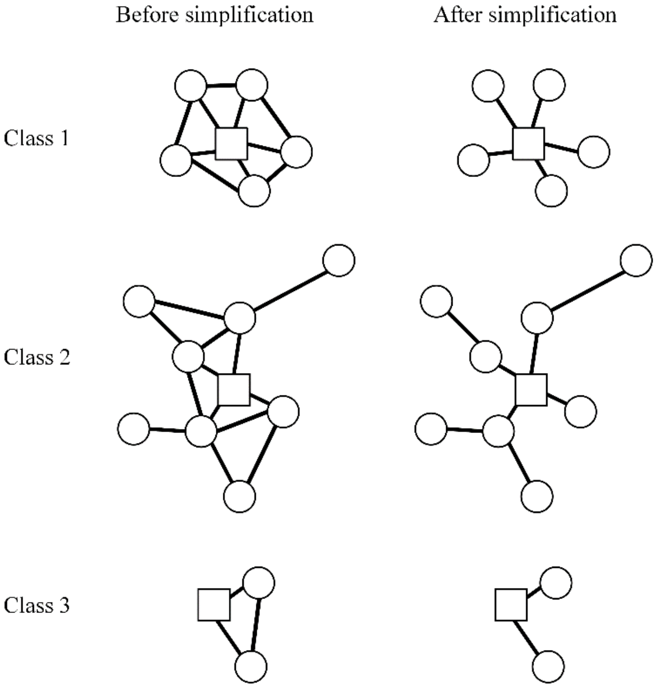

Fig. B2. Simplification result of each class

In Fig. B2, the structure in each class is simplified to be a tree. The edge between any two nodes in each class is weighted by the Euclidean distance on the manifold learned in the section of *Graph construction.* The larger distance is identified between the two nodes, the lower accuracy of the registration between the corresponding images will be obtained. Therefore, the tree structure with the minimum edge weight is a connected graph whose shrinkage will obtain the maximum accuracies of the registrations.

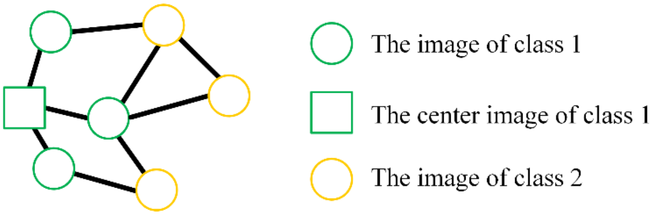

Fig. B3. Structure between the different classes

Between the different classes, structure with cycle is reserved after the simplification. The mesh structure is identified between different classes. Based on the graph displayed in Fig. 2, the mesh structure between class 1 and

2 after simplification is shown in Fig. B3. The mesh structure links more nodes from the different classes than the tree structure. And the corresponding images from the different classes are rapidly driven by the mesh structure towards each other.

Appendix C. Proof of the negative derivative

In the $(k+1)^{\text{th}}$ iteration, images $I_i(k)$ and $I_j(k)$ are warped by $T_i(k)$ and $T_j(k)$, respectively. The resultant images $I_i(k+1)$ and $I_j(k+1)$ is obtained. The deformation $s_{ij}(k+1)$ between $I_i(k+1)$ and $I_j(k+1)$ is concatenated:

$$s_{ij}(k+1)=T_i^{-1}(k)\circ s_{ij}(k)\circ T_j(k) \tag{C.1}$$

According to (9), $T_i^{-1}(k)$ is equal to:

$$T_i^{-1}(k)=\exp(-v_i(k)) \tag{C.2}$$

Substituting (8), (21) and (C.2) to (C.1):

$$\exp(\tilde{v}_{ij}(k+1))=\exp(-v_i(k))\circ\exp(\tilde{v}_{ij}(k))\circ\exp(v_j(k)) \tag{C.3}$$

where $\tilde{v}_{ij}(k+1)$ is the optimal velocity field from $I_i(k+1)$ to $I_j(k+1)$. $v_j(k)$ is the velocity which is computed using (20) for $I_j(k)$.

According to BCH formula [30], $\tilde{v}_{ij}(k+1)$ is:

$$\tilde{v}_{ij}(k+1)=-v_i(k)+\tilde{v}_{ij}(k)+\Psi_{ji}(v_j(k))+\mathrm{O}(v_i(k)) \tag{C.4}$$

where Ψ_{ji} denotes the linearization of the left translation from the space of $v_j(k)$ to $v_i(k)$. Therefore:

$$v_i(k)=-\sum_{i=1}^{N}e''_{ij}\Psi_{ji}(v_j(k)) \tag{C.5}$$

And, given the left-invariant structure of the diffeomorphism group [31], the left invariant metric is obtained for Ψ_{ji}. Therefore:

$$\|v_j(k)\|^2=\|\Psi_{ji}(v_j(k))\|^2 \tag{C.6}$$

Based on $\tilde{v}_{ij}$, the groupwise energy is:

$$div(\text{Groupwise-Energy})=F'(k)=\Delta F(k)=F(k+1)-F(k)=\sum_{i,j=1}^{N}e''_{ij}\left(\|\tilde{v}_{ij}(k+1)\|^2-\|\tilde{v}_{ij}(k)\|^2\right) \tag{C.7}$$

According to (C.4), $\|\tilde{v}_{ij}(k+1)\|^2$ is equal to:

$$\|\tilde{v}_{ij}(k+1)\|^2=\|-v_i(k)+\tilde{v}_{ij}(k)+\Psi_{ji}(v_j(k))+\mathrm{O}(v_i(k))\|^2 \tag{C.8}$$

Substituting (C.8) to (C.7), $\Delta F(k)$ is:

$$\Delta F(k)=\sum_{i,j=1}^{N}e''_{ij}\left(\|-v_i(k)+\tilde{v}_{ij}(k)+\Psi_{ji}(v_j(k))\|^2-\|\tilde{v}_{ij}(k)\|^2\right) \tag{C.9}$$

where $\|\tilde{v}_{ij}(k)\|^2$ and $\|-v_i(k)+\tilde{v}_{ij}(k)+\Psi_{ji}(v_j(k))\|^2$ can be rewritten as $\langle\tilde{v}_{ij}(k),\ \tilde{v}_{ij}(k)\rangle$ and

$\left\langle -v_i(k)+\tilde{v}_{ij}(k)+\Psi_{ji}\left(v_j(k)\right), -v_i(k)+\tilde{v}_{ij}(k)+\Psi_{ji}\left(v_j(k)\right)\right\rangle$. $\langle\cdot,\cdot\rangle$ is the inner product. Through the distributive law, $\left\langle -v_i(k)+\tilde{v}_{ij}(k)+\Psi_{ji}\left(v_j(k)\right), -v_i(k)+\tilde{v}_{ij}(k)+\Psi_{ji}\left(v_j(k)\right)\right\rangle$ is equal to:

$$\begin{aligned}\left\langle -v_i(k)+\tilde{v}_{ij}(k)+\Psi_{ji}\left(v_j(k)\right), -v_i(k)+\tilde{v}_{ij}(k)+\Psi_{ji}\left(v_j(k)\right)\right\rangle &= \left\langle \tilde{v}_{ij}(k), \tilde{v}_{ij}(k)\right\rangle + \\ 2\left\langle \tilde{v}_{ij}(k), -v_i(k)+\Psi_{ji}\left(v_j(k)\right)\right\rangle &+ \left\langle -v_i(k)+\Psi_{ji}\left(v_j(k)\right), -v_i(k)+\Psi_{ji}\left(v_j(k)\right)\right\rangle\end{aligned} \tag{C.10}$$

Substituting (C.10) to (C.9), $\Delta F(k)$ is:

$$\Delta F(k) = 2\underbrace{\sum_{i,j=1}^{N} e''_{ij}\left(\left\langle \tilde{v}_{ij}(k), -v_i(k)+\Psi_{ji}\left(v_j(k)\right)\right\rangle\right)}_{(\mathrm{I})} + \underbrace{\sum_{i,j=1}^{N} e''_{ij}\left(\left\langle -v_i(k)+\Psi_{ji}\left(v_j(k)\right), -v_i(k)+\Psi_{ji}\left(v_j(k)\right)\right\rangle\right)}_{(\mathrm{II})} \tag{C.11}$$

According to (C.5) and (C.6), terms (I) and (II) in (C.11) are calculated:

$$\begin{aligned}(\mathrm{I}) &= -\sum_{i,j=1}^{N} e''_{ij}\left\langle \tilde{v}_{ij}(k), v_i(k)\right\rangle + \sum_{i,j=1}^{N} e''_{ij}\left\langle \tilde{v}_{ij}(k), \Psi_{ji}\left(v_j(k)\right)\right\rangle \\ &= -\sum_{i=1}^{N}\left\langle \sum_{j=1}^{N} e''_{ij}\tilde{v}_{ij}(k), v_i(k)\right\rangle + \sum_{j=1}^{N}\left\langle \sum_{i=1}^{N} e''_{ij}\tilde{v}_{ij}(k), \sum_{i=1}^{N} e''_{ij}\Psi_{ji}\left(v_j(k)\right)\right\rangle \\ &= -\sum_{i=1}^{N}\left\langle \sum_{j=1}^{N} e''_{ij}\tilde{v}_{ij}(k), \sum_{j=1}^{N} e''_{ij}w_{ij}\tilde{v}_{ij}(k)\right\rangle - \sum_{j=1}^{N}\left\langle \sum_{i=1}^{N} e''_{ij}\tilde{v}_{ij}(k), v_i(k)\right\rangle \\ &= -2\sum_{i,j=1}^{N} e''_{ij}w_{ij}\left\|\tilde{v}_{ij}(k)\right\|^2\end{aligned} \tag{C.12}$$

$$\begin{aligned}(\mathrm{II}) &= \sum_{i,j=1}^{N} e''_{ij}\left\|v_i(k)\right\|^2 + \sum_{i,j=1}^{N} e''_{ij}\left\|\Psi_{ji}\left(v_j(k)\right)\right\|^2 - 2\sum_{i,j=1}^{N} e''_{ij}\left\langle v_i(k), \Psi_{ji}\left(v_j(k)\right)\right\rangle \\ &= \sum_{i,j=1}^{N} e''_{ij}w_{ij}^2\left\|\tilde{v}_{ij}(k)\right\|^2 + \sum_{i,j=1}^{N} e''_{ij}\left\|v_i(k)\right\|^2 - 2\sum_{i=1}^{N}\left\langle v_i(k), \sum_{j=1}^{N} e''_{ij}\Psi_{ji}\left(v_j(k)\right)\right\rangle \\ &= 2\sum_{i,j=1}^{N} e''_{ij}w_{ij}^2\left\|\tilde{v}_{ij}(k)\right\|^2 + 2\sum_{i=1}^{N}\left\langle v_i(k), v_i(k)\right\rangle \\ &= 4\sum_{i,j=1}^{N} e''_{ij}w_{ij}^2\left\|\tilde{v}_{ij}(k)\right\|^2\end{aligned} \tag{C.13}$$

Therefore, $\Delta F(k) = -4\left(\sum_{i.j=1}^{N} e''_{ij}w_{ij}\left(1-w_{ij}\right)\left\|\tilde{v}_{ij}(k)\right\|^2\right)$. If I_i is only directly connected to an image I_j, w_{ij} is equal to one; otherwise, $w_{ij}\in(0,1)$. For the groupwise registration, $N\geq 3$, therefore, there is an image linking to multiple images at least in the proposed connected graph G'' and $\sum_{i.,j=1}^{N}\left(1-w_{ij}\right)\in(0,1)$ can not be equal to zero. Given $w_{ij}\in(0,1]$, $\sum_{i.,j=1}^{N}\left(1-w_{ij}\right)\in(0,1)$ and $\left\|\tilde{v}_{ij}(k)\right\|^2>0$, $\Delta F(k)$ and derivative of the groupwise energy are negative.

References:

[1] J. E. Iglesias and M. R. Sabuncu, "Multi-atlas segmentation of biomedical images: A survey," Med. Image Anal., 24, pp. 205-19, (2015).

[2] K. Karasawa, M. Oda, T. Kitasaka, K. Misawa, M. Fujiwara, C. Chu, G. Zheng, D. Rueckert, and K. Mori, "Multi-atlas pancreas segmentation: Atlas selection based on vessel structure," Med. Image Anal., 39, pp. 18-28, (2017).

[3] J. Chang, Z. Tian, W. Lu, X. Gu, M. Chen, and S. B. Jiang, "A novel geometry-dosimetry label fusion method in multi-atlas segmentation for radiotherapy: a proof-of-concept study," Phys. Med. Biol., 62, pp. 3656-3667, (2017).

[4] M. Cabezas, A. Oliver, X. Llado, J. Freixenet, and M. B. Cuadra, "A review of atlas-based segmentation for magnetic resonance brain images," Comput Methods Programs Biomed, 104, pp. e158-77, (2011).

[5] X. Artaechevarria, A. Munoz-Barrutia and C. Ortiz-de-Solorzano, "Combination strategies in multi-atlas image segmentation: application to brain MR data," IEEE Trans Med Imaging, 28, pp. 1266-77, (2009).

[6] S. K. Balci, P. Golland, M. Shenton, and W. M. Wells, "Free-Form B-spline Deformation Model for Groupwise Registration," Med Image Comput Comput Assist Interv, 10, pp. 23-30, (2007).

[7] J. Ashburner and K. J. Friston, "Computing average shaped tissue probability templates," Neuroimage, 45, pp. 333-41, (2009).

[8] H. Wang, M. Rusu, T. Golden, A. Gow, and A. Madabhushi, "Mouse Lung Volume Reconstruction from Efficient Groupwise Registration of Individual Histological Slices with Natural Gradient," in Proceedings of SPIE. vol. 8669, S. Ourselin and D. R. Haynor, Eds., 2013.

[9] H. Jia, G. Wu, Q. Wang, and D. Shen, "ABSORB: Atlas Building by Self-organized Registration and Bundling," Neuroimage, 51, pp. 1057-70, (2010).

[10] S. Joshi, B. Davis, M. Jomier, and G. Gerig, "Unbiased diffeomorphic atlas construction for computational anatomy," Neuroimage, 23 Suppl 1, pp. S151-60, (2004).

[11] M. R. Sabuncu, S. K. Balci, M. E. Shenton, and P. Golland, "Image-driven population analysis through mixture modeling," IEEE Trans Med Imaging, 28, pp. 1473-87, (2009).

[12] G. Wu, H. Jia, Q. Wang, and D. Shen, "SharpMean: groupwise registration guided by sharp mean image and tree-based registration," Neuroimage, 56, pp. 1968-81, (2011).

[13] C. Hoogendoorn, N. Duchateau, D. Sanchez-Quintana, T. Whitmarsh, F. M. Sukno, M. De Craene, K. Lekadir, and A. F. Frangi, "A high-resolution atlas and statistical model of the human heart from multislice CT," IEEE Trans Med Imaging, 32, pp. 28-44, (2013).

[14] Z. Tang and Y. Fan, "Groupwise Image Registration Guided by a Dynamic Digraph of Images," Neuroinformatics, 14, pp. 131-45, (2016).

[15] H. Jia, P. T. Yap, G. Wu, Q. Wang, and D. Shen, "Intermediate templates guided groupwise registration of diffusion tensor images," Neuroimage, 54, pp. 928-39, (2011).

[16] S. Ying, G. Wu, Q. Wang, and D. Shen, "Hierarchical unbiased graph shrinkage (HUGS): a novel groupwise registration for large data set," Neuroimage, 84, pp. 626-38, (2014).

[17] B. B. Devi and V. Sarma, "A fuzzy multistage evolutionary (fume) clustering technique," Pattern Recognition Letter, 2, pp. 139-145, (1984).

[18] T. Vercauteren, X. Pennec, A. Perchant, and N. Ayache, "Symmetric log-domain diffeomorphic Registration: a demons-based approach," Med Image Comput Comput Assist Interv, 11, pp. 754-61, (2008).

[19] J. C. DUNN, "Graph theoretic analysis of pattern-classification via tamuras fuzzy relation," IEEE Transactions on Systems Man and Cybernetics, SMC4, pp. 310-313, (1974).

[20] R. DUBES and A. K. JAIN, "Clustering techniques - Users dilemma," Pattern Recognition, 8, pp. 247-260, (1976).

[21] M. Leone, Sumedha and M. Weigt, "Unsupervised and semi-supervised clustering by message passing: soft-constraint affinity propagation," Eur. Phys. J. B, 66, pp. 125-135, (2008).

[22] R. Souvenir and R. Pless, "Isomap and Nonparametric Models of Image Deformation," in IEEE Workshop on Motion and Video Computing, 2005, pp. 195-200.

[23] R. Pollack, M. Sharir and G. Rote, "Computing the geodesic center of a simple polygon," Discrete Comput. Geom., 4, pp. 611-626, (1989).

[24] T. Heimann, B. van Ginneken, M. A. Styner, Y. Arzhaeva, V. Aurich, C. Bauer, A. Beck, C. Becker, R. Beichel, G. Bekes, F. Bello, G. Binnig, H. Bischof, A. Bornik, P. M. Cashman, Y. Chi, A. Cordova, B. M. Dawant, M. Fidrich, J. D. Furst, D. Furukawa, L. Grenacher, J. Hornegger, D. Kainmuller, R. I. Kitney, H. Kobatake, H. Lamecker, T. Lange, J. Lee, B. Lennon, R. Li, S. Li, H. P. Meinzer, G. Nemeth, D. S. Raicu, A. M. Rau, E. M. van Rikxoort, M. Rousson, L. Rusko, K. A. Saddi, G. Schmidt, D. Seghers, A. Shimizu, P. Slagmolen, E. Sorantin, G. Soza, R. Susomboon, J. M. Waite, A. Wimmer, and I. Wolf, "Comparison and evaluation of methods for liver segmentation from CT datasets," IEEE Trans Med Imaging, 28, pp. 1251-65, (2009).

[25] P. J. Besl and N. D. Mckay, "A method for registration of 3-d shapes," IEEE T. Pattern Anal., 14, pp. 239-256, (1992).

[26] Y. Tian, Q. Chen, W. Wang, Y. Peng, Q. Wang, F. Duan, Z. Wu, and M. Zhou, "A vessel active contour model for vascular segmentation," Biomed Res. Int., 2014, p. 106490, (2014).

[27] A. Schenk, G. Prause and H. O. Peitgen, "Efficient semiautomatic segmentation of 3D objects in medical images," in *Lecture Notes in Computer Science*. vol. 1935, S. Delp, A. M. DiGioia and B. Jaramaz, Eds., 2000, pp. 186-195.

[28] M. Hori, T. Okada, K. Higashiura, Y. Sato, Y. W. Chen, T. Kim, H. Onishi, H. Eguchi, H. Nagano, K. Umeshita, K. Wakasa, and N. Tomiyama, "Quantitative imaging: quantification of liver shape on CT using the statistical shape model to evaluate hepatic fibrosis," Acad. Radiol., 22, pp. 303-9, (2015).

[29] D. C. Barratt, C. S. Chan, P. J. Edwards, G. P. Penney, M. Slomczykowski, T. J. Carter, and D. J. Hawkes, "Instantiation and registration of statistical shape models of the femur and pelvis using 3D ultrasound imaging," Med. Image Anal., 12, pp. 358-74, (2008).

[30] S. Helgason, Differential Geometry, Lie Groups, and Symmetric Spaces (Sigurdur Helgason): Academic Press, 2012.

[31] N. K. Smolentsev, "Diffeomorphism groups of compact manifolds," Journal of Mathematical Sciences, 146, pp. 6213-6312, (2007).

*Graphical Abstract

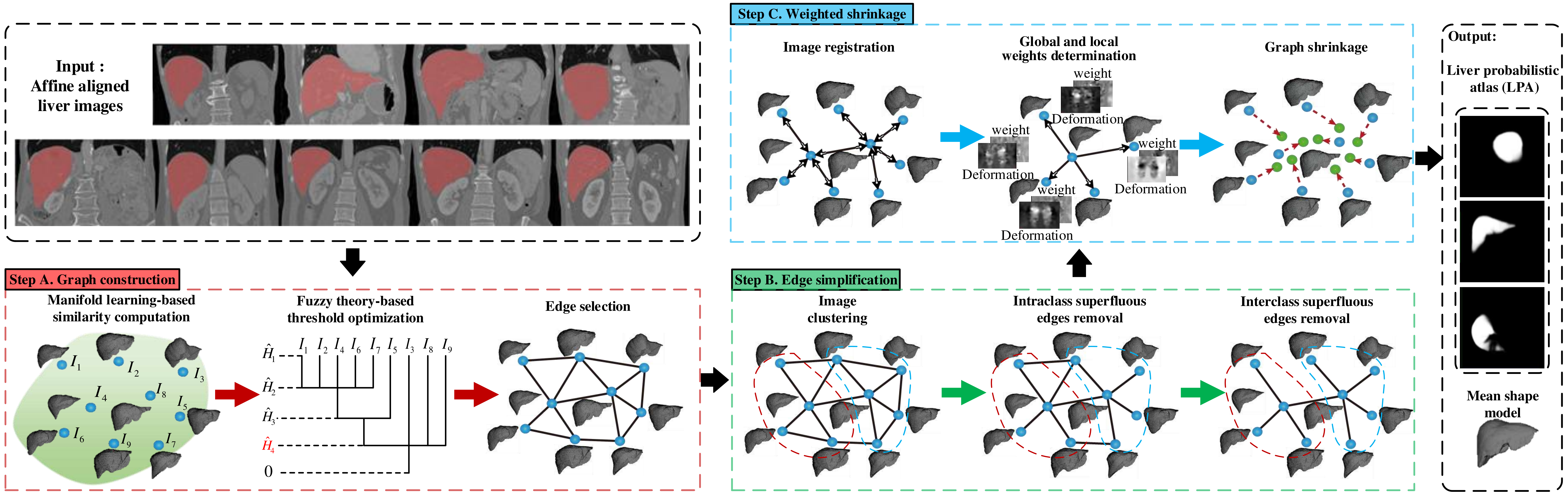

Highlights

- An atlas is constructed based on a graph which is automatically built to model the global distribution of the dataset on the image manifold without a priori templates.
- Higher computational efficiency through requiring fewer edges is achieved by maintaining the local distributions on the image manifold.
- Improved accuracy of the resultant atlas by capturing both global and local variations of each image on the manifold in the graph shrinkage process.
- Compared with six state-of-the-art methods on synthetic and clinical datasets, results of the proposed method show a competitive performance.

***Conflict of Interest Form**

Declaration of interest

The authors declare that they have no competing interests.